



HAL
open science

Object kinetic Monte Carlo modelling of irradiation microstructures with elastic interactions

Thomas Jourdan

► **To cite this version:**

Thomas Jourdan. Object kinetic Monte Carlo modelling of irradiation microstructures with elastic interactions. *Modelling and Simulation in Materials Science and Engineering*, 2022, 30 (8), pp.085013. 10.1088/1361-651X/ac9d57 . cea-03885836

HAL Id: cea-03885836

<https://cea.hal.science/cea-03885836v1>

Submitted on 6 Dec 2022

HAL is a multi-disciplinary open access archive for the deposit and dissemination of scientific research documents, whether they are published or not. The documents may come from teaching and research institutions in France or abroad, or from public or private research centers.

L'archive ouverte pluridisciplinaire **HAL**, est destinée au dépôt et à la diffusion de documents scientifiques de niveau recherche, publiés ou non, émanant des établissements d'enseignement et de recherche français ou étrangers, des laboratoires publics ou privés.

Object kinetic Monte Carlo modelling of irradiation microstructures with elastic interactions

T. Jourdan

Université Paris-Saclay, CEA, Service de Recherches de Métallurgie Physique, 91191, Gif-sur-Yvette, France

E-mail: thomas.jourdan@cea.fr

Abstract.

Elastic interactions between point defects and sinks, such as dislocations and cavities, affect the diffusion of point defects and are responsible for some of the features observed in microstructures under irradiation. It is therefore necessary to include elastic interactions in kinetic simulations for a quantitative prediction of material properties. In this work a method is presented to accurately and efficiently evaluate the strain field in object kinetic Monte Carlo simulations. It can handle any strain field which is biharmonic, such as the one generated by a dislocation segment or a cavity in isotropic elasticity. A speed-up of several orders of magnitude is obtained compared to the direct summation over strain sources, so that simulations over experimental time scales can be performed within reasonable computation times. The case of a thin foil containing a high density of loops under irradiation is investigated. Loop growth rates are found to depend on the loop radius, as shown experimentally, but more complex effects due to the surrounding microstructure are also highlighted.

1 Introduction

2 Microstructure evolution under irradiation is known to be driven by the large
3 supersaturation of vacancies and self-interstitial atoms (SIAs) [1]. These point defects
4 migrate to pre-existing sinks, such as dislocations, grain boundaries and surfaces, or
5 agglomerate with each other, which typically leads to the formation of cavities and
6 dislocation loops. The sustained growth of both vacancy and SIA clusters when
7 only Frenkel pairs are generated by irradiation has been successfully explained by the
8 dislocation bias model [2]. This model relies on the fact that SIAs interact more
9 strongly with elastic fields due to their larger distortion field, and therefore diffuse
10 preferentially towards dislocations and dislocation loops, which create long-range elastic
11 fields compared to cavities. Modelling precisely the diffusion of point defects to the
12 various sinks of the microstructure is therefore important to predict quantitatively the
13 growth rate of dislocation loops and cavities, from which void swelling rates can be
14 deduced [3].

15 Object kinetic Monte Carlo (OKMC) has been successfully used to model the
16 growth kinetics of vacancy and SIA clusters [4, 5, 6, 7, 8]. However, in most cases
17 elastic fields were not taken into account. They were included in OKMC only in a few
18 studies, considering that sinks do not evolve [9, 10, 11, 12, 13, 14], more rarely with
19 full account of sink evolution [15, 16]. To model the preferential absorption of SIAs
20 by dislocations without including the elastic field, a larger absorption region around
21 dislocations is generally adopted regarding SIAs. Beyond this absorption region, point
22 defects perform a pure random walk, *i.e.* the diffusion is not biased by elastic fields. This
23 approach is very efficient, since all jump frequencies are the same whatever the point
24 defect location in the matrix, but it relies on a parameter, the extent of the absorption
25 region, which must be determined by dedicated elastic bias calculations [10, 13]. Elastic
26 biases depend on the temperature, sink size in the case of dislocation loops and cavities,
27 so in general a tedious parametrization task is necessary to cover all relevant cases. In
28 addition biases are assumed not to depend on the surrounding microstructure, which has
29 proven to be erroneous [17, 16]. Taking into account explicitly the elastic interactions in
30 OKMC appears necessary to obtain results in quantitative agreement with experimental
31 results.

32 Performing efficient OKMC simulations with elastic interactions is not an easy task.
33 OKMC relies on the fast evaluation of jump frequencies, which becomes problematic
34 when they depend on the interaction of point defects with the local elastic field.
35 Within linear elasticity, it is convenient to obtain this local field by summing individual
36 contributions of all point defects and sinks in the system. This approach becomes
37 more and more expensive as the number of sinks in the system increases, or if periodic
38 boundary conditions (PBCs) are used. Indeed, due to the long range of the fields
39 generated by dislocations, it is not possible to use a cutoff distance for their evaluation.
40 In practice, it is nearly impossible to reach realistic simulation times if the field changes
41 after each defect jump.

42 Calculations may become considerably more tractable if the strain field of point
43 defects and point defect clusters which are mobile can be neglected. This is usually
44 the case if these mobile objects remain small. For example, in fcc metals Frank loops
45 are immobile and their strain field, within the dipolar approximation, is proportional
46 to the number of SIAs which form them. For typical sizes of several nanometers, it is
47 orders of magnitude larger than the strain field of SIAs or small mobile SIA clusters.
48 Therefore, if the concentration of mobile species is not too high, their contribution to
49 the field can be safely ignored. This assumption will be made in the rest of this work.
50 Since the field is unchanged after the jump of a defect, it may be advantageous to use
51 techniques which evaluate the field on a grid‡. The local field, after each defect jump,
52 can be calculated efficiently by interpolation of the values at the grid points. The field is
53 updated only when the sink microstructure changes, due to the absorption or emission
54 of a mobile species. The calculation of the field on the grid may be costly, so this
55 approach is especially useful when jump events are much more frequent than absorption
56 and emission events by sinks. This is true except at very low temperature (high sink
57 density) and high temperature (high emission rate of defects by sinks).

58 Calculating the field on a grid can be done efficiently by two main techniques.
59 The first one is to solve the problem in Fourier space, using fast Fourier transform
60 (FFT) [18]. It has been done successfully in phase field [19, 20] and discrete dislocation
61 dynamics simulations (DDD) [21, 22]. However this method requires some care to
62 avoid numerical artifacts due to the FFT grid [23]. Since the elastic field can vary
63 quite sharply, in particular close to sinks, a dense grid is required to obtain reliable
64 point defect trajectories in OKMC. This can become unnecessarily expensive for large
65 systems with low sink density.

66 The other technique is the fast multipole method (FMM) [24]. Although it is often
67 used as an order N method to calculate the field at the location of the sources, it gives a
68 local expansion of the field on a grid, which can be used in the present case to evaluate
69 the local field at the position of mobile species. An upper bound for the error on the
70 field can be defined rigorously and an adaptive version of the algorithm [25] permits to
71 reduce the memory footprint and computation time when sources are heterogeneously
72 distributed. Several flavours of the FMM have been used in DDD [26, 27, 28].

73 In this article a method based on the FMM is presented to calculate efficiently
74 the elastic field in OKMC simulations. It enables the simulation of large elastically
75 isotropic systems with common sinks observed in irradiated microstructures (cavities,
76 dislocations, dislocation loops, stacking fault tetrahedra, etc.). We show that this
77 real space approach is particularly convenient to simulate systems with heterogeneous
78 distributions of sinks, or with free surfaces. As an application we simulate the evolution
79 of dislocation loops in aluminum. We show that interstitial loops do not necessarily all

‡ One could even envisage to precalculate the field on all atomic sites. Due to memory constraints, this can only be done on small systems. This method is especially useful when the microstructure does not evolve with time [12]. Otherwise an update of the field on each lattice site is necessary after a change in the microstructure, which may become computationally expensive.

80 grow under irradiation, in contradiction with previous OKMC and rate theory models,
81 but in agreement with experiments.

82 1. OKMC modelling with elastic interactions

83 1.1. Jump frequencies of point defects in presence of an elastic field

84 OKMC is a method which is well adapted to simulate the evolution of microstructures
85 under irradiation. It relies on a database of known events, which are of several types:
86 creation of new defects by irradiation, jump of a point defect from a stable position
87 to another one, thermal emission of a point defect. Events are performed sequentially
88 following the standard residence time algorithm [29, 30]. Elastic interactions between
89 point defects and sinks alter the frequency of events. For example, the jump frequency
90 of a point defect from $\mathbf{x} = (x_1, x_2, x_3)$ to $\mathbf{x} + \mathbf{h}$ can be written as

$$\nu^{\mathbf{h}}(\mathbf{x}) = \nu_0 \exp\left(-\frac{\Delta E^{\mathbf{h}}(\mathbf{x})}{k_{\text{B}}T}\right), \quad (1)$$

91 where ν_0 is an attempt frequency and $\Delta E^{\mathbf{h}}$ is the activation energy, which reads

$$\Delta E^{\mathbf{h}}(\mathbf{x}) = E^{\text{m}} + E^{\text{int,s}}(\mathbf{x} + \mathbf{h}/2) - E^{\text{int,e}}(\mathbf{x}). \quad (2)$$

92 In this expression, E^{m} is the migration energy without elastic interactions, $E^{\text{int,e}}$ and
93 $E^{\text{int,s}}$ are the interaction energies for stable and saddle configurations, respectively. Here
94 the saddle position is assumed to be located halfway between the two stable positions.
95 A similar dependency of emission rates on elastic interactions exists [31] and will not be
96 detailed here.

97 To lowest order, the interaction energy of a point defect with a strain field ε_{ij}
98 depends on the elastic dipole of the point defect P_{ij} [32, 33] (summation on repeated
99 indexes is implied):

$$E^{\text{int}}(\mathbf{x}) = -P_{ij}\varepsilon_{ij}(\mathbf{x}). \quad (3)$$

100 For anisotropic defects, the elastic dipole depends on the defect orientation. It is in
101 general different for stable and saddle configurations.

102 Within linear elasticity, the strain field can be calculated at any point by summing
103 the strain contributions of all objects in the microstructure.

104 1.2. Strain sources

105 As discussed previously, the interaction between point defects or small mobile point
106 defect clusters is not considered in this work. This is in general justified by the fact
107 that the strain field due to large objects is much more intense. There is no difficulty to
108 add this contribution of point defects as dipole-dipole interactions. However, in general
109 the efficiency of the code would be considerably reduced due to the update of the field
110 after any event affecting a point defect. Expressions of strain fields created by three

111 common objects, a dislocation loop, a dislocation segment and a cavity, are recalled in
 112 this section, in the framework of isotropic elasticity. The shear modulus and Poisson's
 113 ratio are noted μ and ν , respectively. Only the solution in an infinite medium is given;
 114 surface effects are treated in Section 3.2.

115 *1.2.1. Dislocation segment and dislocation loop* We follow the approach by Ghoniem
 116 and Sun [34] to give explicit expressions for the strain. To derive the strain field, we
 117 start from Mura's formula, which expresses the derivative of the displacement field \mathbf{u}
 118 created by a dislocation loop [35, 36] as a line integral over the perimeter of the loop \mathcal{C}
 119 (see also Fig. 1):

$$\frac{\partial u_i}{\partial x_j} = u_{i,j} = \epsilon_{jnh} b_m C_{pqmn} \oint_{\mathcal{C}} \frac{\partial}{\partial x_q} G_{ip}^{\infty}(\mathbf{x} - \mathbf{x}') dx'_h, \quad (4)$$

120 where ϵ_{ijk} is the permutation tensor, \mathbf{b} is the Burgers vector, G_{ij}^{∞} is the elastic Green
 121 function in an infinite body, and C_{ijkl} are the elastic constants.

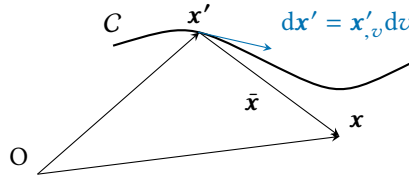


Figure 1. Notations used for a curved dislocation \mathcal{C} .

122 For an isotropic material, the elastic Green function is given by ($\bar{\mathbf{x}} = \mathbf{x} - \mathbf{x}'$,
 123 $\bar{x} = |\bar{\mathbf{x}}|$):

$$G_{ij}^{\infty}(\bar{\mathbf{x}}) = \frac{1}{16\pi(1-\nu)\mu} \left(\delta_{ij} \frac{3-4\nu}{\bar{x}} + \frac{\bar{x}_i \bar{x}_j}{\bar{x}^3} \right) = \frac{1}{4\pi\mu} \frac{\delta_{ij}}{\bar{x}} - \frac{1}{16\pi\mu(1-\nu)} \frac{\partial^2}{\partial x_i \partial x_j} \bar{x}. \quad (5)$$

124 In this equation δ_{ij} is the Kronecker delta.

125 Elastic constants can be written as

$$C_{pqmn} = \mu (\delta_{pm} \delta_{qn} + \delta_{pn} \delta_{qm}) + \frac{2\nu\mu}{1-2\nu} \delta_{pq} \delta_{mn}, \quad (6)$$

126 and since $\varepsilon_{ij} = 1/2 (u_{i,j} + u_{j,i})$ the strain reads [34]:

$$\varepsilon_{ij}(\bar{\mathbf{x}}) = \frac{1}{8\pi} \oint_{\mathcal{C}} \left[-\frac{1}{2} (\epsilon_{jkl} b_l \bar{x}_{,i} + \epsilon_{ikl} b_l \bar{x}_{,j} - \epsilon_{ikl} b_l \bar{x}_{,i} - \epsilon_{jkl} b_l \bar{x}_{,j})_{,pp} + \frac{\epsilon_{kmn} b_n \bar{x}_{,mij}}{1-\nu} \right] dx'_k. \quad (7)$$

127 The parametric form of $\mathbf{x}'(v)$ given by Ghoniem and Sun is used:

$$\mathbf{x}'(v) = \mathbf{q}_i \mathcal{N}_i(v), \quad (8)$$

128 where $\mathcal{N}_i(v)$ are basis functions, v is a parameter and \mathbf{q}_i are generalized coordinates.

129 The differential reads

$$dx'_k = x'_{k,v} dv = q_{ik} \mathcal{N}_{i,v}(v) dv. \quad (9)$$

Using quadrature to evaluate the integral, the strain can be numerically computed by summing over a finite number of strain sources:

$$\varepsilon_{ij}(\bar{\mathbf{x}}) \approx \frac{1}{8\pi} \sum_{\alpha=1}^{N_q} w_{\alpha} \left[-\frac{1}{2} (\epsilon_{jkl} b_i \bar{x}_{,l} + \epsilon_{ikl} b_j \bar{x}_{,l} - \epsilon_{ikl} b_l \bar{x}_{,j} - \epsilon_{jkl} b_l \bar{x}_{,i})_{,pp} (v_{\alpha}) + \frac{\epsilon_{kmn} b_n \bar{x}_{,mij} (v_{\alpha})}{1-\nu} \right] x'_{k,v} (v_{\alpha}), \quad (10)$$

where N_q is the number of quadrature points and w_{α} are the quadrature weights. In the following Gauss-Legendre quadrature is used.

This expression can be simplified, since some terms are zero and $\bar{x}_{,ijk}$ is invariant by permutation. The expressions can be given, for example, as a function of $\bar{x}_{,111}$, $\bar{x}_{,112}$, $\bar{x}_{,113}$, $\bar{x}_{,123}$, $\bar{x}_{,221}$, $\bar{x}_{,222}$, $\bar{x}_{,223}$, $\bar{x}_{,331}$, $\bar{x}_{,332}$ and $\bar{x}_{,333}$ (similar simplifications were performed for the stress in [34]). Explicit expressions of the strain components are given in Appendix A.

For a circular dislocation loop of radius r , located at the origin, and whose normal to its habit plane is \mathbf{n} , the following coordinates can be chosen:

$$\mathbf{q}_1 = r \begin{pmatrix} \frac{n_2^2}{1+n_3} + n_3 \\ -\frac{n_1 n_2}{1+n_3} \\ -n_1 \end{pmatrix} \quad \mathbf{q}_2 = r \begin{pmatrix} \frac{-n_1 n_2}{1+n_3} \\ \frac{n_1^2}{1+n_3} + n_3 \\ -n_2 \end{pmatrix} \quad (11)$$

and the basis functions are ($v \in [-1, 1]$ for Gauss-Legendre quadrature)

$$\mathcal{N}_1(v) = \cos(\pi v) \quad \mathcal{N}_2(v) = \sin(\pi v). \quad (12)$$

Expression (10) can also be used for a dislocation segment. In this case,

$$\mathbf{q}_1 = \mathbf{x}_1 \quad \mathbf{q}_2 = \mathbf{x}_2, \quad (13)$$

where \mathbf{x}_1 and \mathbf{x}_2 are the end points of the segment and the basis functions are ($v \in [-1, 1]$)

$$\mathcal{N}_1(v) = \frac{1}{2}(1-v) \quad \mathcal{N}_2(v) = \frac{1}{2}(1+v). \quad (14)$$

1.2.2. Cavity Let us consider a cavity of radius r , which contains some gas with pressure p , located at \mathbf{x}' . The strain field created by this cavity in the matrix, at \mathbf{x} ($\bar{x} > r$), is [37, 38]

$$\varepsilon_{ij}(\bar{\mathbf{x}}) = \left(p - \frac{2\hat{\gamma}}{r} \right) \frac{1}{4\mu} \left(\frac{r}{\bar{x}} \right)^3 \left[\delta_{ij} - 3 \frac{\bar{x}_i \bar{x}_j}{\bar{x}^2} \right], \quad (15)$$

where $\hat{\gamma}$ is the surface tension of the metal.

It can also be written under the following form, which is more convenient for use in the FMM:

$$\varepsilon_{ij}(\bar{\mathbf{x}}) = - \left(p - \frac{2\hat{\gamma}}{r} \right) \frac{1}{4\mu} r^3 \frac{\partial^2}{\partial x'_i \partial x'_j} \left(\frac{1}{\bar{x}} \right). \quad (16)$$

Contrary to the dislocation segment and the dislocation loop, the strain is calculated exactly by using a single strain source located at \mathbf{x}' .

153 2. Fast calculation of the strain field

154 2.1. Calculation of the field using local expansions and FMM

155 Following Eq. (16), any component of the strain field generated by a cavity can be
156 written as a derivative of $1/\bar{x}$, so it is harmonic. A general solution to $\Delta\phi = 0$ is

$$\phi(\mathbf{x}) = \sum_{l=0}^{\infty} \sum_{m=-l}^l \left(L_{lm} x^l Y_l^m(\theta, \varphi) + M_{lm} \frac{Y_l^m(\theta, \varphi)}{x^{l+1}} \right) \quad (17)$$

$$= \sum_{l=0}^{\infty} \sum_{m=-l}^l (L_{lm} R_l^m(x, \theta, \varphi) + M_{lm} I_l^m(x, \theta, \varphi)), \quad (18)$$

157 where Y_l^m are the spherical harmonics (see Appendix B, Eq. (B.1)), R_l^m and I_l^m are the
158 regular and irregular solid harmonics, respectively. If the strain field is evaluated at \mathbf{x}
159 with $x < x'$, multipole expansion coefficients M_{lm} are all zero and only local expansion
160 coefficients L_{lm} are useful. In this case Eq. (18) is called a local expansion. It can be
161 truncated to a given value of l to give an approximate value of the strain field.

162 The strain field generated by a dislocation segment depends on the derivatives of \bar{x}
163 (Eq. (7)), so it is not harmonic in general. However, \bar{x} is a solution to the biharmonic
164 equation. This is also the case of its derivatives. Any solution ψ to the biharmonic
165 equation can be written as [39]

$$\psi(\mathbf{x}) = \phi(\mathbf{x}) + x^2\omega(\mathbf{x}), \quad (19)$$

166 where ϕ and ω are harmonic functions. So for a microstructure containing dislocations
167 and cavities, if all strain sources are such that $x' > x$, any strain field component can
168 be evaluated by a local expansion of the following type:

$$\psi(\mathbf{x}) = \sum_{l=0}^{\infty} \sum_{m=-l}^l L_{lm}^{(0)} R_l^m(x, \theta, \varphi) + x^2 \sum_{l=0}^{\infty} \sum_{m=-l}^l L_{lm}^{(2)} R_l^m(x, \theta, \varphi). \quad (20)$$

169 Compared to a Taylor expansion of the field, this decomposition is more compact: if
170 the summation is performed up to order p , the number of terms is $O(p^2)$, whereas a
171 cartesian expansion requires $O(p^3)$ terms. Since a fast evaluation of the local expansion
172 is crucial in the KMC algorithm, using spherical harmonics is particularly interesting.

173 The FMM offers a rigorous framework to evaluate a field using local expansions with
174 a prescribed accuracy. It is based on a hierarchical set of boxes forming a mesh, which
175 can be uniform or adaptive. In the adaptive version, boxes are sub-divided in child boxes
176 until the number of sources in each box is lower than a threshold n_{\max} . The case of a
177 uniform mesh is shown schematically in Fig. 2. The field at \mathbf{x} , inside box b , is obtained
178 by summing two terms. The first one is a local expansion as in Eq. (20), which contains
179 the contribution of all sources located in boxes “well separated” from b (in blue). In
180 particular, it contains information on periodic images of the simulation box and more
181 generally on boundary conditions (see section 3). The second term is a direct sum over

182 the other sources (in orange), using expressions (10) and (15). Using local expansions
 183 only for boxes which are well separated from b ensures that local expansions converge.
 184 Cubic boxes are considered well separated if they do not share a boundary point. In
 185 this case, the minimal distance between the centers of boxes is $d_{\min} = 2/\sqrt{3}(r_b + r_b)$,
 186 where r_b is the radius of the smallest sphere enclosing b . This worst case can be used to
 187 define well-separated boxes when they are not cubic, by imposing that they are distant
 188 from each other by at least d_{\min} . It is the criterion used in our FMM implementation,
 189 which handles non-cubic boxes.

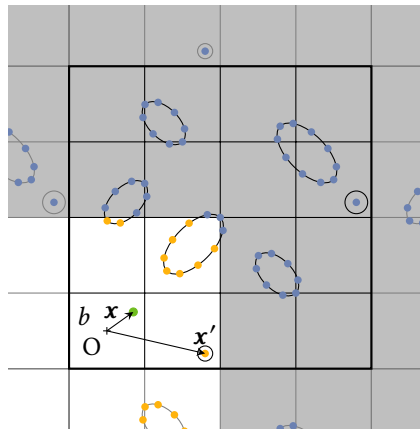


Figure 2. Schematic view of the calculation of the strain field using FMM in a microstructure containing dislocation loops and cavities. The contribution of blue sources, located in boxes which are well-separated from box b , containing the target point, is accounted for in a local expansion whose origin is the center of b . The contribution of other sources (in orange) is calculated with expressions (10) and (15).

190 The core of the FMM is the fast determination of local expansions. It relies on
 191 operations on multipole expansions of the fields. Once they are calculated for childless
 192 boxes, multipole expansions are translated and merged at lower levels of the hierarchy
 193 (upward pass) and converted into local expansions. Local expansions are then translated
 194 until they are expressed with respect to the center of childless boxes (downward pass).
 195 Details can be found, for example, in Ref. [25].

196 The FMM for harmonic fields, based on expansions in spherical harmonics, has
 197 been amply discussed [24, 40]. In particular, it has been optimised to speed up the
 198 conversion of multipole expansions into local expansions, using rotation of expansions
 199 and exponential representations [25]. For biharmonic fields, Gumerov and Duraiswami
 200 have proposed a modified version of the FMM, based on the decomposition in harmonic
 201 fields given in Eq. (19) [39]. This algorithm uses the classical operations on harmonic
 202 fields and includes an additional step due to the x^2 factor in Eq. (19). Since the definition
 203 of spherical harmonics in the present work differs from the one they used, translation
 204 and conversion formulas are given in Appendix C. The version implemented in this work
 205 includes rotation of expansions [41].

206 The FMM requires the calculation of multipole expansions of the field created by

207 a set of sources. In addition, for the adaptive version, which is used here, calculation of
 208 local expansions directly from sources is also necessary. Coefficients of the expansions
 209 are given for cavities and dislocation segments in the following sections.

210 2.2. Multipole expansion for a cavity

211 To obtain the multipole expansion of the strain field generated by a cavity, it is
 212 convenient to use the following expansion of the coulombic potential [42]:

$$\frac{1}{\bar{x}} = \sum_{l=0}^{\infty} \sum_{m=-l}^l x'^l Y_l^{-m}(\theta', \varphi') \frac{Y_l^m(\theta, \varphi)}{x^{l+1}} = \sum_{l=0}^{\infty} \sum_{m=-l}^l R_l^{-m}(x', \theta', \varphi') I_l^m(x, \theta, \varphi). \quad (21)$$

213 Inserting this expression in Eq. (16) yields the following multipole expansion for the
 214 strain field of a cavity:

$$\varepsilon_{ij}(\mathbf{x}) = \sum_{l=0}^{\infty} \sum_{m=-l}^l M_{lm} I_l^m(x, \theta, \varphi), \quad (22)$$

215 with

$$M_{lm} = - \left(p - \frac{2\hat{\gamma}}{r} \right) \frac{1}{4\mu} r^3 \frac{\partial^2}{\partial x'_i \partial x'_j} R_l^{-m}(x', \theta', \varphi'). \quad (23)$$

216 Second derivatives of regular solid harmonics are given in Appendix E.

217 2.3. Local expansion for a cavity

218 Coefficients of the local expansion are obtained straightforwardly from the previous
 219 section: the strain field reads

$$\varepsilon_{ij}(\mathbf{x}) = \sum_{l=0}^{\infty} \sum_{m=-l}^l L_{lm} R_l^m(x, \theta, \varphi), \quad (24)$$

220 with

$$L_{lm} = - \left(p - \frac{2\hat{\gamma}}{r} \right) \frac{1}{4\mu} r^3 \frac{\partial^2}{\partial x'_i \partial x'_j} I_l^{-m}(x', \theta', \varphi'). \quad (25)$$

221 Second derivatives of irregular solid harmonics are given in Appendix D.

222 2.4. Multipole expansion for a dislocation segment

223 As can be seen from Eq. (10), the multipole expansion of the strain field of a dislocation
 224 segment is readily deduced from the expansion of $\bar{x}_{,ijk}$. Since \bar{x} is a solution to the
 225 biharmonic equation, it can be expressed as in Eq. (19) [39]. With our convention for
 226 spherical harmonics, we have, for $x > x'$:

$$\begin{aligned} \bar{x} = & \sum_{l=0}^{\infty} \sum_{m=-l}^l \frac{1}{2l+3} x'^2 R_l^{-m}(x', \theta', \varphi') I_l^m(x, \theta, \varphi) \\ & + x^2 \sum_{l=0}^{\infty} \sum_{m=-l}^l \frac{-1}{2l-1} R_l^{-m}(x', \theta', \varphi') I_l^m(x, \theta, \varphi). \end{aligned} \quad (26)$$

227 The derivatives $\bar{x}_{,ijk} = -\bar{x}_{,i'j'k'}$ can thus be written under the following form:

$$\bar{x}_{,ijk} = \sum_{l=0}^{\infty} \sum_{m=-l}^l M_{lm}^{(0)} I_l^m(x, \theta, \varphi) + x^2 \sum_{l=0}^{\infty} \sum_{m=-l}^l M_{lm}^{(2)} I_l^m(x, \theta, \varphi), \quad (27)$$

with

$$M_{lm}^{(0)} = -\frac{1}{2l+3} \frac{\partial^3}{\partial x'_i \partial x'_j \partial x'_k} (x'^2 R_l^{-m}(x', \theta', \varphi')) \quad (28)$$

$$M_{lm}^{(2)} = \frac{1}{2l-1} \frac{\partial^3}{\partial x'_i \partial x'_j \partial x'_k} (R_l^{-m}(x', \theta', \varphi')). \quad (29)$$

228 Derivatives of regular solid harmonics in Appendix E may be used to obtain more
229 convenient expressions of multipole expansion coefficients.

230 2.5. Local expansion for a dislocation segment

231 As for multipole expansions, local expansions can be calculated from the following
232 expression of \bar{x} (for $x < x'$):

$$\begin{aligned} \bar{x} = \sum_{l=0}^{\infty} \sum_{m=-l}^l \frac{-x'^2}{2l-1} I_l^{-m}(x', \theta', \varphi') R_l^m(x, \theta, \varphi) \\ + x^2 \sum_{l=0}^{\infty} \sum_{m=-l}^l \frac{1}{2l+3} I_l^{-m}(x', \theta', \varphi') R_l^m(x, \theta, \varphi). \end{aligned} \quad (30)$$

233 The local expansion of $\bar{x}_{,ijk} = -\bar{x}_{,i'j'k'}$ is

$$\bar{x}_{,ijk} = \sum_{l=0}^{\infty} \sum_{m=-l}^l L_{lm}^{(0)} R_l^m(x, \theta, \varphi) + x^2 \sum_{l=0}^{\infty} \sum_{m=-l}^l L_{lm}^{(2)} R_l^m(x, \theta, \varphi), \quad (31)$$

with

$$L_{lm}^{(0)} = \frac{1}{2l-1} \frac{\partial^3}{\partial x'_i \partial x'_j \partial x'_k} (x'^2 I_l^{-m}(x', \theta', \varphi')) \quad (32)$$

$$L_{lm}^{(2)} = -\frac{1}{2l+3} \frac{\partial^3}{\partial x'_i \partial x'_j \partial x'_k} (I_l^{-m}(x', \theta', \varphi')). \quad (33)$$

234 Derivatives of irregular solid harmonics in Appendix D may be used to obtain more
235 convenient expressions of local expansion coefficients.

236 2.6. Comparison with other FMM approaches for isotropic elasticity

237 The FMM has already been used to calculate elastic fields generated by dislocation
238 ensembles. The first implementation for three dimensional DDD used expansions in
239 cartesian coordinates [26]. As previously discussed, this approach is not optimal here

240 since local expansions are evaluated with $O(p^3)$ operations. On the contrary, the
 241 evaluation of an expansion in regular solid harmonics requires only $O(p^2)$ operations.

242 The FMM based on spherical harmonics, which was initially developed for the
 243 harmonic potential $1/\bar{x}$, has been used for other interaction potentials. Fu *et al.* [43]
 244 showed that harmonic FMM can be used for interaction potentials of the form

$$\mathcal{F}(\mathcal{Q}(\mathbf{x}')/\bar{x}, \mathbf{x}), \quad (34)$$

245 where \mathcal{Q} is a function depending on data related to sources only and \mathcal{F} is a linear
 246 operator on $\mathcal{Q}(\mathbf{x}')/\bar{x}$. In general several harmonic FMM calls must be combined to
 247 generate the field. In practice, some identities are useful to write potentials depending
 248 on derivatives of \bar{x} , such as the elastic Green function and its derivatives, under the form
 249 given by Eq. (34) [43, 44]. For example, the third derivatives can be written as [27]:

$$\bar{x}_{,ijk} = \left(x_k \frac{\partial^2}{\partial x_i \partial x_j} + \delta_{jk} \frac{\partial}{\partial x_i} + \delta_{ki} \frac{\partial}{\partial x_j} \right) \left(\frac{1}{\bar{x}} \right) - \frac{\partial^2}{\partial x_i \partial x_j} \left(\frac{x'_k}{\bar{x}} \right). \quad (35)$$

250 From Eq. (10), the strain field generated by a single source on a dislocation segment
 251 can be expressed as

$$\varepsilon_{ij}(\bar{\mathbf{x}}) = q_{rst}^{ij} \bar{x}_{,rst}. \quad (36)$$

252 Inserting Eq. (35) into Eq. (36), we obtain:

$$\varepsilon_{ij}(\bar{\mathbf{x}}) = \left(x_t \frac{\partial^2}{\partial x_r \partial x_s} + \delta_{st} \frac{\partial}{\partial x_r} + \delta_{rt} \frac{\partial}{\partial x_s} \right) \left(\frac{q_{rst}^{ij}}{\bar{x}} \right) - \frac{\partial^2}{\partial x_s \partial x_t} \left(\frac{q_{rst}^{ij} x'_t}{\bar{x}} \right). \quad (37)$$

253 It can be seen that without any optimisation, the calculation of one component of the
 254 strain field requires 36 harmonic FMM calls (27 for q_{rst}^{ij}/\bar{x} and 9 for $q_{rst}^{ij} x'_t/\bar{x}$). This
 255 is significantly more expensive than the approach adopted here, which requires only 2
 256 harmonic calls per component. Recently, Chen *et al.* [28] used the same decomposition
 257 of \bar{x} as Fu *et al.* [43] to develop an FMM for the calculation of the stress field induced by
 258 dislocation segments. However no details concerning the implementation were provided.

259 The number of FMM calls is limited in our approach because the derivatives are
 260 taken with respect to the source variables x'_i instead of the target variables x_i (see
 261 Eqs. (22)-(23) and (27)-(29)). A similar technique was already used for the calculation of
 262 the magnetic field generated by magnetic dipoles [45]. Another advantage of this method
 263 is that any harmonic or biharmonic field can be included in the present formalism
 264 without requiring additional FMMs. If the derivatives are taken on the target variables
 265 and if the fields are not derived the same way, one must keep track of the nature of the
 266 sources, thereby increasing the number of FMMs.

267 3. Periodic boundary conditions and free surfaces

268 In OKMC simulations, PBCs may be used for self-defect migration, in order to simulate
 269 the microstructure evolution in the bulk of large systems, where the effect of free surfaces

270 or grain boundaries can be locally neglected. Accordingly, the contribution of the elastic
 271 fields from the sources in the image boxes must be summed to provide the field due to
 272 a periodic layout of strain sources. We describe in section 3.1 how to perform this
 273 summation efficiently with FMM and to ensure that it converges to a correct value.

274 Considering some boundaries of the simulation box as free surfaces is another
 275 interesting case. This situation is representative of thin foils observed in transmission
 276 electron microscopy, which are a few hundred nanometers thick. The above expressions
 277 of the strain field induced by cavities and dislocation segments correspond to isolated
 278 defects in an infinite medium. A correction to the elastic field calculated by FMM is
 279 necessary to ensure that it corresponds to a system with free surfaces (section 3.2).

280 3.1. Periodic boundary conditions: removing the spurious dipolar contribution

281 To sum the contributions of periodic images, we extend the upward pass of the FMM
 282 to lower “macroscopic” levels of hierarchy and obtain the multipole expansions of larger
 283 and larger clusters of the initial simulation box [46]. The downward pass is performed
 284 from macroscopic levels down to the highest levels of hierarchy, with interaction lists
 285 containing boxes located in image simulation boxes. This simple method permits to add
 286 the elastic field of a large number of periodic image boxes at low computation cost.

287 However, it is known that the field obtained by direct summation over image boxes is
 288 not necessarily absolutely convergent. In some cases the value of the sum depends on the
 289 way the summation is performed and may not correspond to a periodic solution [47]. For
 290 example, let us consider the strain fields created by dislocation loops and cavities, which
 291 decay as $1/\bar{x}^3$ for large values of \bar{x} . The summation is only conditionally convergent if it
 292 is performed along the three directions of space. Cai *et al.* have shown that the strain
 293 field corresponding to a periodic solution $\varepsilon_{ij}^{\text{PBC}}$ differs from the field obtained by direct
 294 summation by a constant field ε^0 [47]:

$$\varepsilon_{ij}(\mathbf{x}) = \varepsilon_{ij}^{\text{PBC}}(\mathbf{x}) + \varepsilon_{ij}^0. \quad (38)$$

295 This means that the displacement field resulting from the same summation procedure
 296 has two spurious components, a linear one and a constant one:

$$u_i(\mathbf{x}) = u_i^{\text{PBC}}(\mathbf{x}) + \mathbf{g}_i \cdot \mathbf{x} + u_i^0, \quad (39)$$

297 where u_i^{PBC} is the periodic displacement field, \mathbf{g}_i and u_i^0 are a constant vector and a
 298 constant scalar, respectively. The constant field ε^0 , which must be subtracted from ε ,
 299 is deduced from \mathbf{g}_i :

$$\varepsilon_{ij}^0 = \frac{1}{2}(g_{ij} + g_{ji}). \quad (40)$$

300 The constant vector \mathbf{g}_i can be computed by evaluating the displacement field (39) at one
 301 corner of the box and at the three adjacent corners. Although this method is simple and
 302 general, it is rather cumbersome in the present context, since with the FMM we only
 303 have access to the strain field. The evaluation of the displacement field would require
 304 to develop an additional FMM, which we want to avoid.

305 Recently it has been shown that for a box containing an elastic dipole component
306 but no monopole term, the field $\boldsymbol{\varepsilon}^0$ can be written in the following explicit form [48]:

$$\varepsilon_{ij}^0(\mathbf{x}) = \frac{1}{2} \int_{\mathcal{S}} p_{lk} n_k [G_{il,j}^{\infty}(\bar{\mathbf{x}}) + G_{jl,i}^{\infty}(\bar{\mathbf{x}})] dS', \quad (41)$$

307 where $\mathbf{p} = \mathbf{P}/V$, with \mathbf{P} the elastic dipole tensor of the system and V the volume of
308 the simulation box, \mathbf{n} the outward-pointing normal to the integration surface \mathcal{S} . This
309 surface delimits the domain over which the direct summation over strain sources is
310 performed. Actually, since the function to integrate varies as $1/\bar{x}^2$, the integral does not
311 depend on the domain itself, but only on its shape. The summation domain must be
312 sufficiently large to fully account for higher order terms, which are absolutely convergent.
313 In practice, using 2 to 3 macroscopic levels in FMM is enough. The field $\boldsymbol{\varepsilon}^0$ is calculated
314 at the center of the simulation box. In isotropic elasticity, it is convenient to use the
315 analytical form given in Ref. [48] and recalled in Appendix F.

316 Removing $\boldsymbol{\varepsilon}^0$ amounts to simulating a finite macroscopic system under loading given
317 by $\boldsymbol{\sigma} = -\mathbf{p}$ [48]. This means that to simulate a physical system with free surfaces, this
318 loading should be removed. Finally the strain in a macroscopic system with free surfaces
319 is obtained from the FMM field $\boldsymbol{\varepsilon}^{\text{FMM}}$ through

$$\boldsymbol{\varepsilon}(\mathbf{x}) = \boldsymbol{\varepsilon}^{\text{FMM}}(\mathbf{x}) - \boldsymbol{\varepsilon}^0 + \mathbf{S}\mathbf{p}, \quad (42)$$

320 where \mathbf{S} is the compliance matrix, *i.e.* the inverse of the stiffness matrix (see Eq. (6)):

$$S_{ijkl} = \frac{1}{4\mu} (\delta_{ik}\delta_{jl} + \delta_{il}\delta_{jk}) - \frac{\nu}{2\mu(1+\nu)} \delta_{ij}\delta_{kl}. \quad (43)$$

321 Tensor \mathbf{p} remains to be determined. During the upward pass of the FMM, the
322 multipole expansion of the field generated by all objects in the simulation box is
323 calculated, so the strain field can be written as

$$\varepsilon_{ij}(\mathbf{x}) = \sum_{l=0}^p \sum_{m=-l}^l M_{lm}^{ij,(0)} \frac{Y_l^m(\theta, \varphi)}{x^{l+1}} + x^2 \sum_{l=0}^p \sum_{m=-l}^l M_{lm}^{ij,(2)} \frac{Y_l^m(\theta, \varphi)}{x^{l+1}}. \quad (44)$$

324 Far from the simulation box, one must recover the strain field of an elastic dipole,
325 decaying as $1/x^3$. This means that $M_{2m}^{ij,(0)}$ and $M_{4m}^{ij,(2)}$ are related to the total elastic
326 dipole in the simulation box. The displacement field induced by an elastic dipole \mathbf{P}
327 located at the origin in the middle of the box is [49]

$$u_i^{\text{dip}}(\mathbf{x}) = -G_{ij,k}^{\infty}(\mathbf{x}) P_{jk} \quad (45)$$

$$= -\frac{1}{16\pi\mu(1-\nu)} \left[-2(1-2\nu) \frac{x_k}{x^3} P_{ik} + \frac{x_i}{x^3} \text{Tr}(\mathbf{P}) - 3 \frac{x_i x_k x_l}{x^5} P_{lk} \right], \quad (46)$$

328 from which the strain field is obtained:

$$\begin{aligned} \varepsilon_{ij}^{\text{dip}}(\mathbf{x}) = & -\frac{1}{16\pi\mu(1-\nu)} \left[-2(1-2\nu)\frac{P_{ij}}{x^3} \right. \\ & + \frac{x^2\delta_{ij} - 3x_ix_j}{x^5} \text{Tr}(\mathbf{P}) \\ & - 6\nu\frac{x_i}{x^5} (x_k P_{jk}) \\ & - 6\nu\frac{x_j}{x^5} (x_k P_{ik}) \\ & \left. + 3\frac{5x_ix_j - \delta_{ij}x^2}{x^7} x_k x_l P_{kl} \right]. \end{aligned} \quad (47)$$

329 From this expression, one can evaluate the multipole expansion coefficients $M_{20}^{ij,(0)}$ (see
330 Eq. (B.3))

$$M_{20}^{ij,(0)} = \int_0^{2\pi} \int_0^\pi \frac{5}{4\pi} \varepsilon_{ij}^{\text{dip}}(\mathbf{x}) x^3 (Y_2^0(\theta, \varphi))^* \sin\theta \, d\theta d\varphi. \quad (48)$$

331 This leads to the following linear system:

$$M_{20}^{11,(0)} = \frac{1}{16\pi\mu(1-\nu)} \left[\frac{4}{7}(4-7\nu)P_{11} - \frac{4}{7}P_{22} + \frac{2}{7}P_{33} \right] \quad (49)$$

$$M_{20}^{22,(0)} = \frac{1}{16\pi\mu(1-\nu)} \left[-\frac{4}{7}P_{11} + \frac{4}{7}(4-7\nu)P_{22} + \frac{2}{7}P_{33} \right] \quad (50)$$

$$M_{20}^{33,(0)} = \frac{1}{16\pi\mu(1-\nu)} \left[\frac{2}{7}P_{11} + \frac{2}{7}P_{22} - \frac{8}{7}(4-7\nu)P_{33} \right] \quad (51)$$

$$M_{20}^{23,(0)} = -\frac{1}{16\pi\mu(1-\nu)} \frac{2}{7}(5-7\nu)P_{23} \quad (52)$$

$$M_{20}^{13,(0)} = -\frac{1}{16\pi\mu(1-\nu)} \frac{2}{7}(5-7\nu)P_{13} \quad (53)$$

$$M_{20}^{12,(0)} = \frac{1}{16\pi\mu(1-\nu)} \frac{4}{7}(5-7\nu)P_{12}. \quad (54)$$

332 This system is underdetermined for $\nu = 1/2$ or $\nu = 4/7$. In practice $\nu < 1/2$ so it can
333 be safely used to calculate the dipole tensor associated to the simulation box and thus
334 \mathbf{p} .

335 3.2. Free surfaces

336 The elastic Green function given in Eq. (5) is only valid for an infinite medium. If some
337 boundaries of the simulation box correspond to a free surface, the strain field calculated
338 with this Green function may be erroneous. Unphysical forces \mathbf{T} may appear at the
339 surface if some objects are too close to it. In order to obtain the correct elastic solution,
340 we adopt the method proposed by van der Giessen and Needleman [50]. They add a
341 field which cancels surface tractions produced by the solution in an infinite medium.

342 This field is the solution of the following equations:

$$\nabla \cdot \boldsymbol{\sigma} = 0 \quad \text{in } \mathcal{V} \quad (55)$$

$$\boldsymbol{\sigma} \cdot \mathbf{n} = -\mathbf{T} \quad \text{on } \mathcal{S}^f, \quad (56)$$

343 where \mathcal{V} is the domain corresponding to the simulation box, \mathcal{S}^f its free surfaces, \mathbf{n} is
 344 the outward normal vector to \mathcal{S}^f . Although surface tractions can vary steeply, the field
 345 induced by these forces smoothen with depth. An adaptive mesh is therefore particularly
 346 adapted to solve these equations. The finite element method (FEM) can be easily used
 347 with adaptive meshes, which makes this method particularly interesting in this context.
 348 It is based on the variational formulation of problem (55)-(56) [51]: we must find \mathbf{u} such
 349 that

$$\int_{\mathcal{V}} \boldsymbol{\sigma}(\mathbf{u}) : \boldsymbol{\varepsilon}(\mathbf{v}) \, dV = - \int_{\mathcal{S}^f} \mathbf{T} \cdot \mathbf{v} \, dS \quad \forall \mathbf{v} \in H^1, \quad (57)$$

350 with \mathbf{u} the displacement field to be found, \mathbf{v} a vector test function and H^1 the Sobolev
 351 space of vector functions. The colon operator is the inner product between two tensors,
 352 *i.e.* $\boldsymbol{\sigma} : \boldsymbol{\varepsilon} = \sigma_{ij} \varepsilon_{ij}$. Since there is no Dirichlet boundary condition (on \mathbf{u}), the solution is
 353 not unique. If free surfaces are considered in the three directions of space, *i.e.* with pure
 354 Neumann boundary conditions, any rigid body motion, given by (with \mathbf{a} , \mathbf{b} constant
 355 vectors)

$$\mathbf{u}(\mathbf{x}) = \mathbf{a} \times \mathbf{x} + \mathbf{b}, \quad (58)$$

356 can be added to the solution ($\boldsymbol{\varepsilon}(\mathbf{u}) = 0$). The space of rigid body motions RM consists
 357 of translations and rotations, and for a pure Neumann problem, it is of dimension 6.

358 A unique solution can be found by setting the displacement of some points to
 359 zero [52]. Here we use Lagrange multipliers [51] to impose that the solution is
 360 linearly independent of functions in RM . This leads to the following saddle point
 361 problem [51, 53]: we must find $(\mathbf{u}, \boldsymbol{\lambda})$, with \mathbf{u} in H^1 and $\boldsymbol{\lambda}$ in RM , such that

$$\int_{\mathcal{V}} \boldsymbol{\sigma}(\mathbf{u}) : \boldsymbol{\varepsilon}(\mathbf{v}) \, dV + \int_{\mathcal{V}} \mathbf{v} \cdot \boldsymbol{\lambda} \, dV = - \int_{\mathcal{S}^f} \mathbf{T} \cdot \mathbf{v} \, dS \quad \forall \mathbf{v} \in H^1 \quad (59)$$

$$\int_{\mathcal{V}} \mathbf{u} \cdot \boldsymbol{\mu} \, dV = 0 \quad \forall \boldsymbol{\mu} \in RM. \quad (60)$$

362 The number of rigid body motions to be blocked depends on the number of surfaces. The
 363 three translation motions must always be included in the rigid motions to be blocked;
 364 however the three rotations must be included only if the simulation box has free surfaces
 365 along the three directions of space. If PBCs are used along one direction, only the
 366 rotation around this direction must be blocked, so the null space of rigid body motions
 367 is of dimension 4. If PBCs are used along two directions, only translations must be
 368 considered and the null space is only of dimension 3. In practice, problem (59)-(60) was
 369 solved using the open-source software FEniCS [54].

370 The mesh to be used in FEM calculations can be fixed at the beginning of an
 371 OKMC simulation, but this is not always optimal in terms of efficiency and accuracy.

372 If strain sources remain far from surfaces, spatial variations of surface tractions are
 373 gentle and a coarse mesh can be used near surfaces without loss of accuracy, resulting in
 374 highly efficient FEM solving. If strain sources get closer to the surface as the simulation
 375 proceeds, surface tractions are expected to vary much more steeply and the mesh should
 376 be locally refined. Refining the mesh only where it is necessary is important to keep
 377 the FEM solving efficient. The adaptive FMM provides a rather natural way to do so.
 378 Since the FMM box size depends on the local density of sources, steep variations of the
 379 traction field resulting from sources close to the surface are expected to be accompanied
 380 with a local decrease of the FMM box size. Accordingly, we set the typical size of
 381 FEM elements at the surface proportional to the size of FMM boxes. In addition, the
 382 number of surface traction evaluations is set the same for all FMM boxes, resulting in a
 383 higher density of evaluations where FMM boxes are smaller. A schematical view of the
 384 FMM/FEM coupling is shown in Fig. 3.

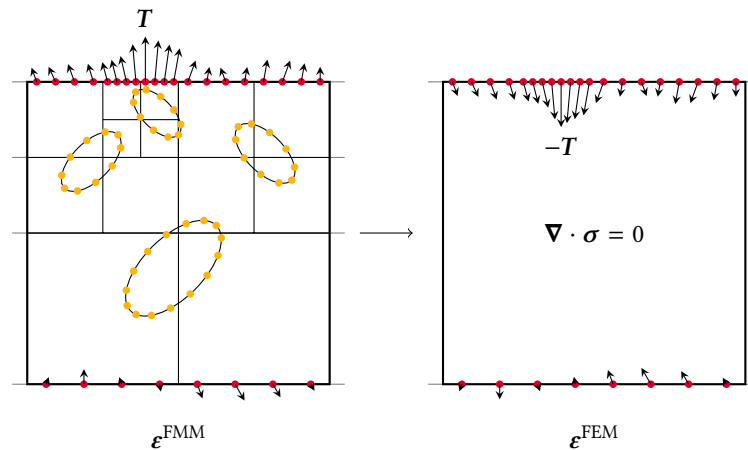


Figure 3. Coupling of adaptive FMM and FEM to obtain the solution compatible with traction-free upper and lower boundaries. The solution in an infinite medium is first obtained, using FMM (ϵ^{FMM}). The adaptive grid is used to evaluate traction forces T on surfaces. Then the solution at mechanical equilibrium under prescribed traction forces $-T$ is determined with FEM (ϵ^{FEM}). The solution of the initial problem is $\epsilon = \epsilon^{\text{FMM}} + \epsilon^{\text{FEM}}$.

385 We chose the open-source software Gmsh [55] to generate the FEM mesh. This mesh
 386 is updated as infrequently as possible, only when the FMM adaptive mesh is modified.
 387 Otherwise, only surface tractions are re-evaluated before the FEM solving. Between two
 388 successive FEM solvings with the same mesh, the solutions are not expected to vary
 389 much and it is advantageous to re-use the solution from a preceding solving as an initial
 390 guess if an iterative solver is used. If a direct solver is employed, it is useful to re-use
 391 the LU factorization.

392 4. Numerical results

393 In this section we present a few test cases, to assess the accuracy and performance of the
 394 method, and to highlight its capabilities. All tests are performed in aluminum at room
 395 temperature. Parameters, which are taken from Ref. [13], are reminded in Table 1.

Table 1. Material parameters for aluminum

Parameter	Symbol	Value
Lattice parameter	a_0	0.405 nm
Atomic volume	Ω	$a_0^3/4 = 0.0167 \text{ nm}^3$
Poisson's ratio	ν	0.35
Shear modulus	μ	26 GPa
Burgers vector (Frank loops)	\mathbf{b}	$a_0[111]/3$
Capture radius of dislocations	r_c	0.47 nm
Migration energy of vacancies	E_v^m	0.605 eV
Migration energy of SIAs	E_i^m	0.105 eV
Attempt frequency	ν_0	10^{13} Hz
Elastic dipole of vacancies at stable position	\mathbf{P}_v^e	$\begin{bmatrix} -3.238 & 0 & 0 \\ 0 & -3.238 & 0 \\ 0 & 0 & -3.238 \end{bmatrix} \text{ eV}$
Elastic dipole of vacancies at saddle position (jump in [110] direction)	\mathbf{P}_v^s	$\begin{bmatrix} -2.866 & -0.080 & 0 \\ -0.080 & -2.866 & 0 \\ 0 & 0 & 1.000 \end{bmatrix} \text{ eV}$
Elastic dipole of SIAs at stable position ([100] orientation)	\mathbf{P}_i^e	$\begin{bmatrix} 19.652 & 0 & 0 \\ 0 & 18.518 & 0 \\ 0 & 0 & 18.518 \end{bmatrix} \text{ eV}$
Elastic dipole of SIAs at saddle position (jump in [110] direction)	\mathbf{P}_i^s	$\begin{bmatrix} 19.498 & 1.133 & 0 \\ 1.133 & 19.498 & 0 \\ 0 & 0 & 19.034 \end{bmatrix} \text{ eV}$

396 4.1. Accuracy and performance of the method

397 The truncation of expansions to order p limits the accuracy of the method. The error
 398 on any component of the strain field can be conveniently estimated by the L^2 relative
 399 error norm [25, 39]:

$$e_2 = \left(\frac{\sum_{k=1}^n |\varepsilon^{\text{direct}}(\mathbf{x}_k) - \varepsilon^{\text{FMM}}(\mathbf{x}_k)|^2}{\sum_{k=1}^n |\varepsilon^{\text{direct}}(\mathbf{x}_k)|^2} \right)^{1/2}, \quad (61)$$

400 where the indexes of the strain component have been dropped for the sake of clarity. The
 401 strain field component ε^{FMM} is calculated by FMM, with expansions truncated to order

402 p . A direct summation over all strain sources is performed to evaluate $\varepsilon^{\text{direct}}$, which is
 403 our reference value. The location of the n strain field evaluations (with $n = 10^4$ here) is
 404 chosen randomly in the matrix, outside the absorption region of sinks. In the test case
 405 considered here, sinks are Frank loops of the same radius, equal to 5 nm. Each loop is
 406 modelled as a collection of straight dislocation segments of maximum length equal to
 407 1 nm. The absorption regions are cylinders of radius $r_c = 2b$, where $b = |\mathbf{b}|$, centered
 408 on the dislocation segments. A total of 40 loops, randomly placed in a cubic system of
 409 edge length 200 nm, generate the strain field. Neither periodic boundary conditions nor
 410 coupling with FEM are considered.

411 The relative error on ε_{11} is shown in Fig. 4 as a function of truncation order p . It
 412 steadily decreases with increasing order. Since the computation cost increases with p ,
 413 its value should be chosen as small as possible. In general, a value of e_2 lower than 10^{-2}
 414 is unnecessary, so in the following $p = 7$ is adopted.

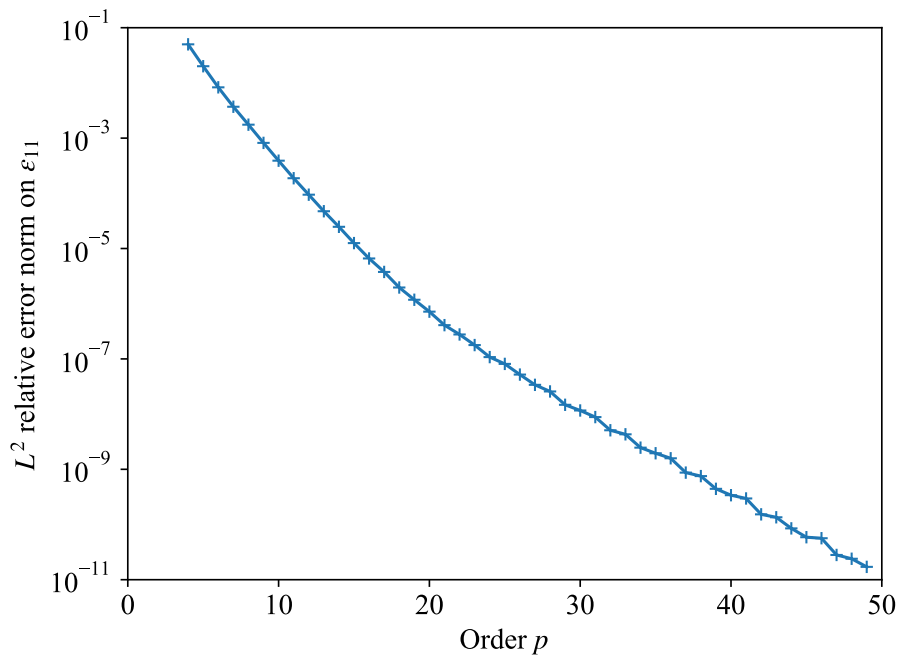


Figure 4. L^2 relative error norm on component ε_{11} as a function of the order p of the multipole and local expansions in the FMM. The system is cubic, of size 200 nm. It contains 40 Frank dislocation loops of 5 nm radius. The error is calculated on $n = 10^4$ points located outside the absorption region of loops.

415 The main purpose of using FMM is to reduce the computation time for the
 416 evaluation of the strain field. Computation times obtained with a direct calculation
 417 and with FMM, assuming that the expansions are up to date, are shown in Fig. 5-(a).
 418 The system is the same as before, but the number of loops, or equivalently the number of
 419 strain sources, is varied. The highest number of loops considered (100 loops) corresponds
 420 to loop densities typically seen in irradiated materials ($\sim 10^{22} \text{ m}^{-3}$). The computation

421 time with the direct approach increases linearly with the number of sources and reaches
422 values of more than 10^{-3} s for 100 loops. When the FMM is used, the computation
423 time is reduced by a factor of around 500 in this high density case. With the FMM,
424 the field is calculated as the sum of two contributions. The first one includes sources
425 which are sufficiently far from the box containing the target point. It is evaluated with
426 a local expansion to order p . The associated computation time is independent of the
427 number of sources. The second contribution is due to the remaining sources, which are
428 too close to the box containing the target point to be included in the local expansion.
429 In the adaptive FMM, they are taken into account with a multipole expansion if the
430 box containing the sources is sufficiently far from the target and if it has a large number
431 of sources. Otherwise, a direct summation on sources is performed (orange sources in
432 Fig. 2). This second contribution explains the increase in computation time with the
433 number of loops. If the maximum number of sources per box is reduced from 70 to 30,
434 additional levels are introduced and in general, the number of sources which contribute
435 to the direct sum decreases. That is why the computation time also decreases. The case
436 of a uniform FMM, with a box size equal to 5 nm, is also reported in Fig. 5-(a). If the
437 number of loops is small, boxes containing target points are most often surrounded by
438 boxes with no sources. The computational cost corresponds to the evaluation of a local
439 expansion. Once the number of loops is sufficiently large to populate the boxes around
440 each target point, the computation time increases because of the direct summation.

441 As a first approximation, PBCs can be introduced in the direct approach by
442 summing the contributions of sources located in the first neighbour shell of periodic
443 images. This is not a bad approximation if PBCs are used along at most two directions,
444 since the sum is absolutely convergent in this case (see Section 3.1). The computation
445 time when PBCs are set along two directions corresponds to the dashed black line in
446 Fig. 5-(a). As expected, it is around 9 times higher than without PBCs. With FMM,
447 the computation time only marginally increases, because the number of sources on
448 which the direct summation is performed only increases for target points located close
449 to the boundaries of the system. This is a clear advantage of the FMM over the direct
450 calculation.

451 Up to now it has been assumed that multipole and local expansions are up to date.
452 Each time a sink absorbs or emits a point defect, expansions must be updated. We
453 see in Fig. 5-(b) that with our version of the FMM, which is not fully optimized, the
454 calculation of multipole and local expansions for all strain components can be up to a few
455 seconds for dense microstructures. It increases if n_{\max} decreases, since additional levels
456 are introduced. We have seen that on the contrary, reducing n_{\max} speeds up the field
457 evaluation. So n_{\max} must be adjusted to minimize the sum of the two contributions
458 to the computation time. Empirically, $n_{\max} = 70$ appears to be satisfactory with
459 the present implementation. We also see in Fig. 5-(b) that considering PBCs hardly
460 affects the time to update expansions, so that the global computation time is nearly
461 independent of PBCs with FMM. As in Fig. 5-(a), the computation time for the uniform
462 FMM is reported. With such a small box size of 5 nm, the update of expansions takes

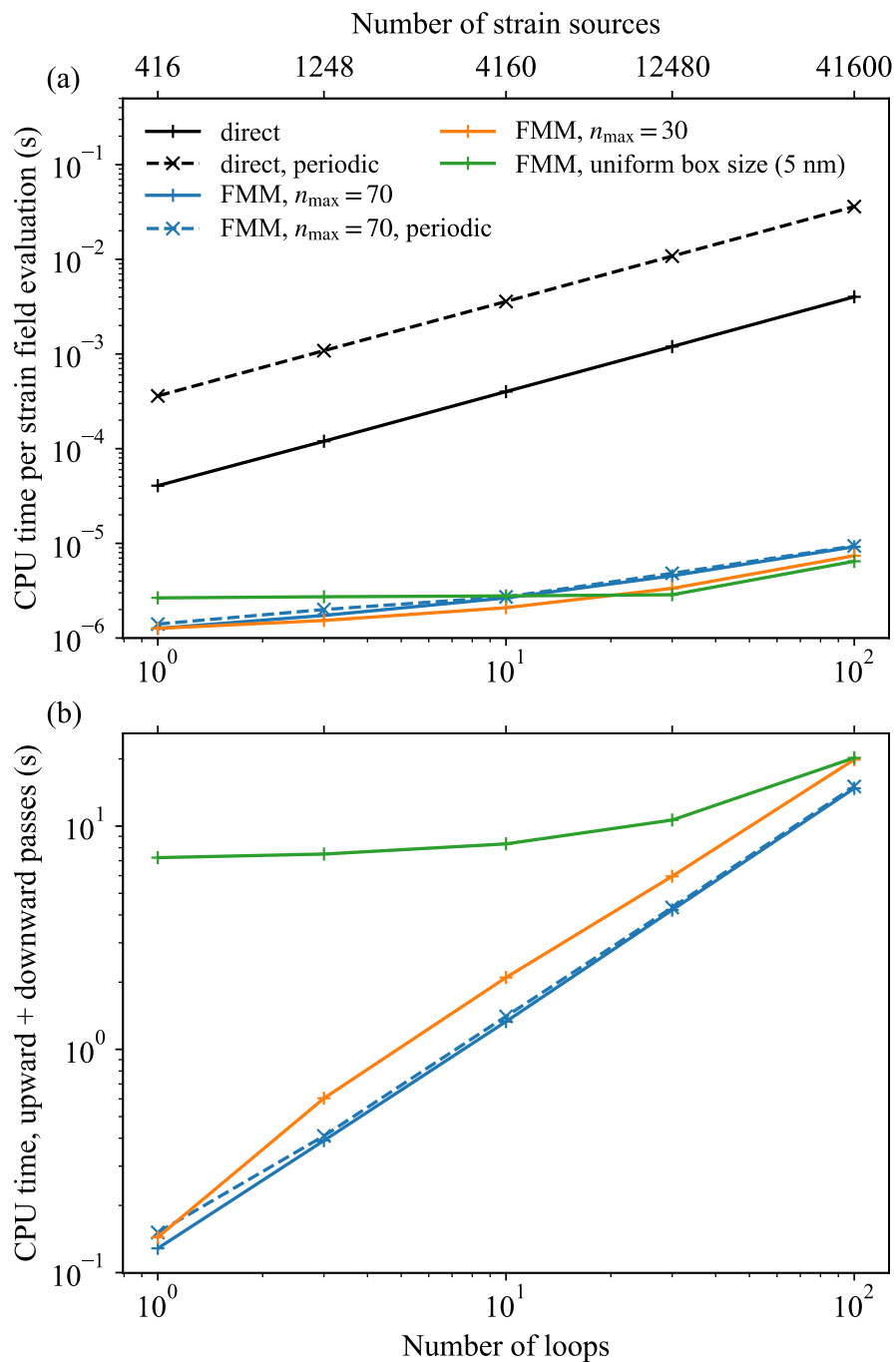


Figure 5. (a) Computation time for one strain field evaluation, for direct and FMM calculations, as a function of the number of loops in a $(200 \text{ nm})^3$ system. Loops have a radius of 5 nm. Dashed curves refer to periodic calculations along two directions. Periodic images are only partially accounted for in the direct calculation, by including the first neighbour shell (8 images boxes). The adaptive version of the FMM is used with two different criteria for the division of boxes ($n_{\max} = 30$ and $n_{\max} = 70$). The green curve corresponds to a FMM calculation with a 5 nm uniform mesh. (b) Computation time for the initial evaluation of local expansions by FMM.

463 much more time than with the adaptive FMM. Although the box size can be tuned
 464 to obtain satisfactory performance, it becomes difficult to do so when the number of
 465 sources evolves appreciably with time. This is typically the case under irradiation, with
 466 the nucleation and growth of clusters. So in general the adaptive version should be
 467 preferred.

468 Since the update of FMM expansions takes significant time, the FMM is useful
 469 only if defects perform a large number of jumps n between two absorption or emission
 470 events. The speed-up is then

$$s = \frac{(z + 1)nt_{\text{direct}}}{(z + 1)nt_{\text{FMM}} + t_{\text{update}}}, \quad (62)$$

471 where t_{direct} and t_{FMM} are the computation time per evaluation of strain field (Fig. 5-
 472 (a)) in the direct and FMM approaches, respectively, and t_{update} is the time required
 473 to update FMM expansion coefficients (Fig 5-(b)). The factor $(z + 1)$ accounts for the
 474 z possible jumps a defect can perform (8 for an SIA, 12 for a vacancy), because an
 475 estimation of the field is necessary for each saddle point. In addition the interaction
 476 energy for the initial stable configuration must be calculated. To evaluate n , let us
 477 consider absorption events only and neglect elastic interactions. The average number of
 478 jumps of a defect before absorption is [56]

$$n = \frac{12}{k^2 a_0^2}, \quad (63)$$

479 where the sink strength is assumed to be the one of a concentration C of loops of radius
 480 r and capture radius r_c [57]:

$$k^2 = \frac{4\pi^2 r}{\ln\left(\frac{8r}{r_c}\right)} C. \quad (64)$$

481 For one loop in the simulation box, we obtain around $n = 10^7$ jumps before absorption,
 482 while for 100 loops, n is around 10^5 . From results shown in Fig. 5, the resulting speed-
 483 up for a system with PBCs in two directions is around 250 for one loop and 1700 for
 484 100 loops. The proportion of time taken for the update of FMM expansion coefficients
 485 increases with the number of loops, so that $(z+1)nt_{\text{FMM}} \approx t_{\text{update}}$ for 100 loops. However,
 486 the time for direct evaluation of the field also increases rapidly with the number of loops.
 487 This results in a larger speed-up if the number of loops increases.

488 A more precise estimation of the speed-up is obtained by measuring the average
 489 CPU time per KMC time step directly in a kinetic simulation. This measurement also
 490 takes into account a variety of other operations occurring during a KMC time step, such
 491 as the computation of energy, the handling of collisions between defects, etc. Previous
 492 microstructures are taken as starting configurations. They evolve following the creation
 493 of Frenkel pairs at a rate of 10^{-4} dpa/s. Results are shown in Fig. 6. The speed-up is
 494 similar to the previous estimation, from two to three orders of magnitude depending on
 495 the number of loops in the system. As before, the update of FMM expansion coefficients
 496 takes a larger proportion of the computation time as the number of loops increases. We

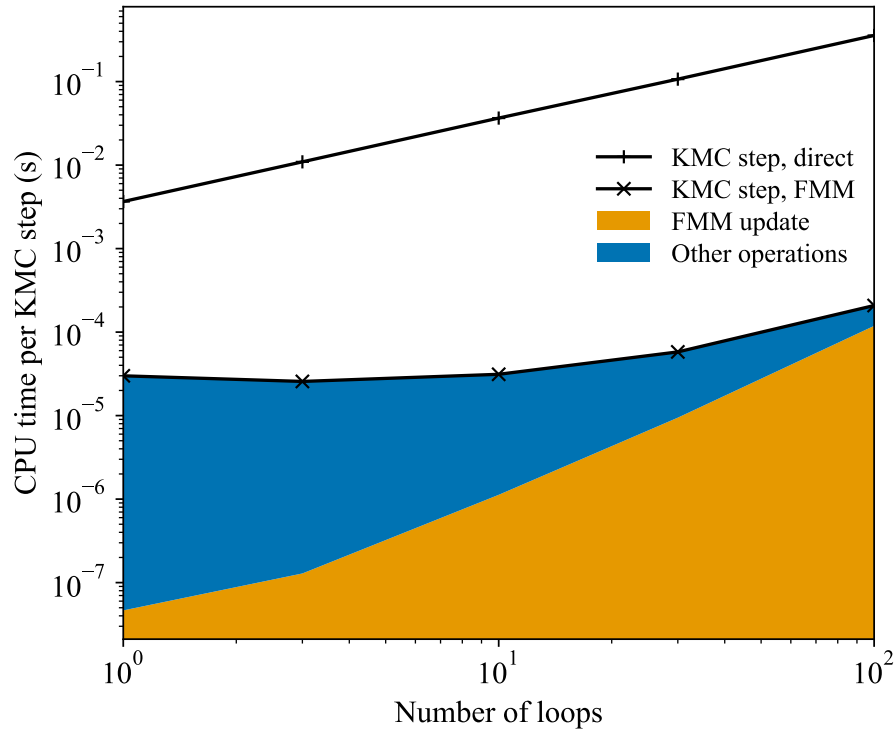


Figure 6. Computation time per KMC step as a function of the number of loops in a $(200 \text{ nm})^3$ system. Loops have a radius of 5 nm. Direct and FMM calculation of the strain field are shown in black solid lines. For FMM, the orange colour area indicates the proportion of time spent in the update of FMM expansion coefficients, other operations being represented in blue.

497 note that in these simulations, we avoid recalculating all multipole expansion coefficients
 498 each time an absorption event occurs. Only boxes whose sources have changed have their
 499 multipole expansions updated. Then only necessary multipole-to-local operations are
 500 performed, which saves computation time.

501 4.2. Impact of free surface on dislocation loop growth

502 In the vicinity of a surface, the growth rate of clusters is altered, because a proportion
 503 of point defects is absorbed by this sink instead of contributing to cluster evolution.
 504 This leads, for example, to the presence of void and loop denuded zones [58, 59, 60].
 505 This effect has been investigated with standard OKMC [61]. With the present method
 506 it is possible to study a more subtle effect, related to the strain field generated by
 507 clusters. We have seen in section 3.2 that if a cluster is located close to a surface, the
 508 associated strain field does not correspond to the field generated in an infinite medium,
 509 since surfaces must be traction-free. The resulting modified energy landscape impacts
 510 the diffusion paths of point defects and thus may change the cluster behaviour.

511 In the following we consider a system with free surfaces along \mathbf{e}_3 , containing a loop

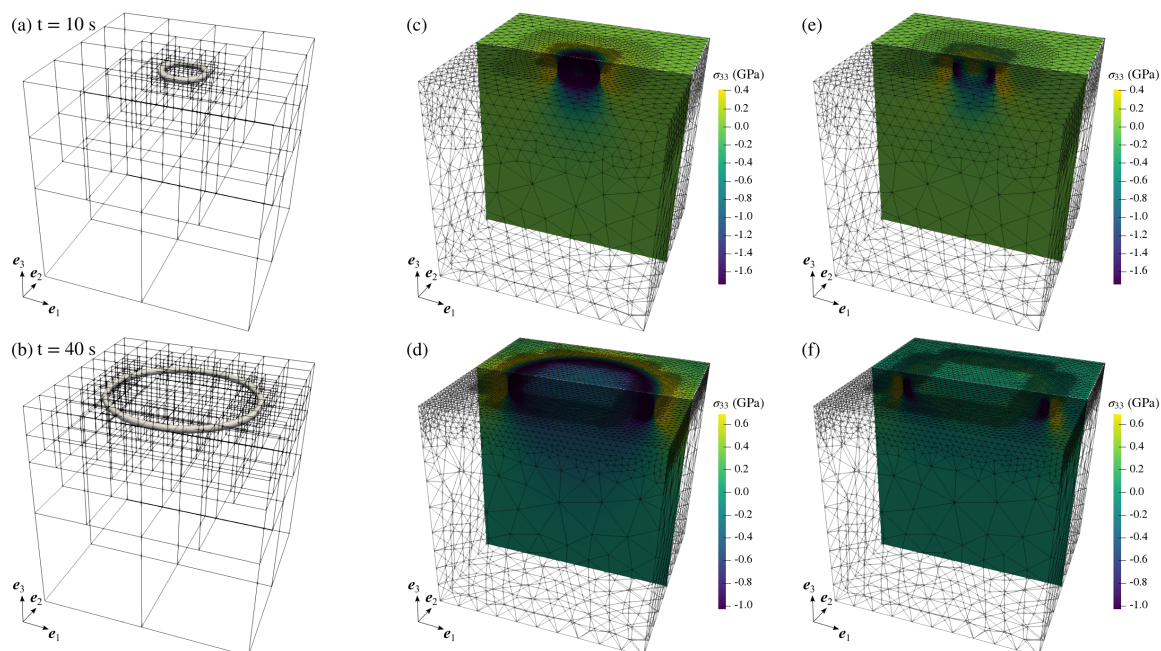


Figure 7. Visualization of the computation of the strain field produced by a dislocation loop located at 2 nm from the upper surface of a $(30 \text{ nm})^3$ system, at (a,c,e) $t = 10 \text{ s}$ and (b,d,f) $t = 40 \text{ s}$. (a,b) Adaptive FMM mesh. (c,d) Component σ_{33} induced by the presence of the loop, if the solution in an infinite medium is used. This solution leads to significant traction forces \mathbf{T} on the upper surface. (e,f) Component σ_{33} when the FEM solution of the mechanical equilibrium with prescribed forces $-\mathbf{T}$ is added to the infinite medium solution.

512 nucleus at a variable distance d from the upper surface. PBCs are used in the two other
 513 directions. The loop nucleus is an interstitial cluster containing 11 SIAs ($r = 0.5 \text{ nm}$),
 514 which is assumed to be immobile and to grow as a Frank loop oriented parallel to
 515 the surface. The dimensions of the system are $30 \text{ nm} \times 30 \text{ nm} \times 30 \text{ nm}$. SIAs and
 516 vacancies are inserted as Frenkel pairs at a dose rate of $5 \times 10^{-3} \text{ dpa/s}$. A view of the
 517 FMM adaptive mesh at two different times is given in Fig. 7-(a,b). The region where
 518 the mesh is refined correlates with the position of the dislocation line. Following the
 519 coupling scheme proposed in Fig. 3, this mesh refinement leads to a fine FEM mesh at
 520 the upper surface close to the dislocation line, where the field varies steeply (Fig. 7-
 521 (c,d)). In the case shown in Fig. 7, which corresponds to a dislocation loop 2 nm away
 522 from the upper surface, traction forces created by the solution in a infinite medium can
 523 be larger than 1 GPa. When the FEM solution of the mechanical equilibrium with
 524 opposite traction forces is added, traction forces are substantially reduced. We see that
 525 this induces a significant change in the stress inside the material (Fig. 7-(e,f)).

526 The evolution of loop size with time is shown in Fig. 8, including or not the
 527 compensation of traction forces. 20 simulations have been performed for distances to
 528 the surface ranging from 2 to 15 nm. One sees that except when the loop is very close
 529 to the surface ($d = 2 \text{ nm}$), the image field correction has only a small influence on loop
 530 growth.

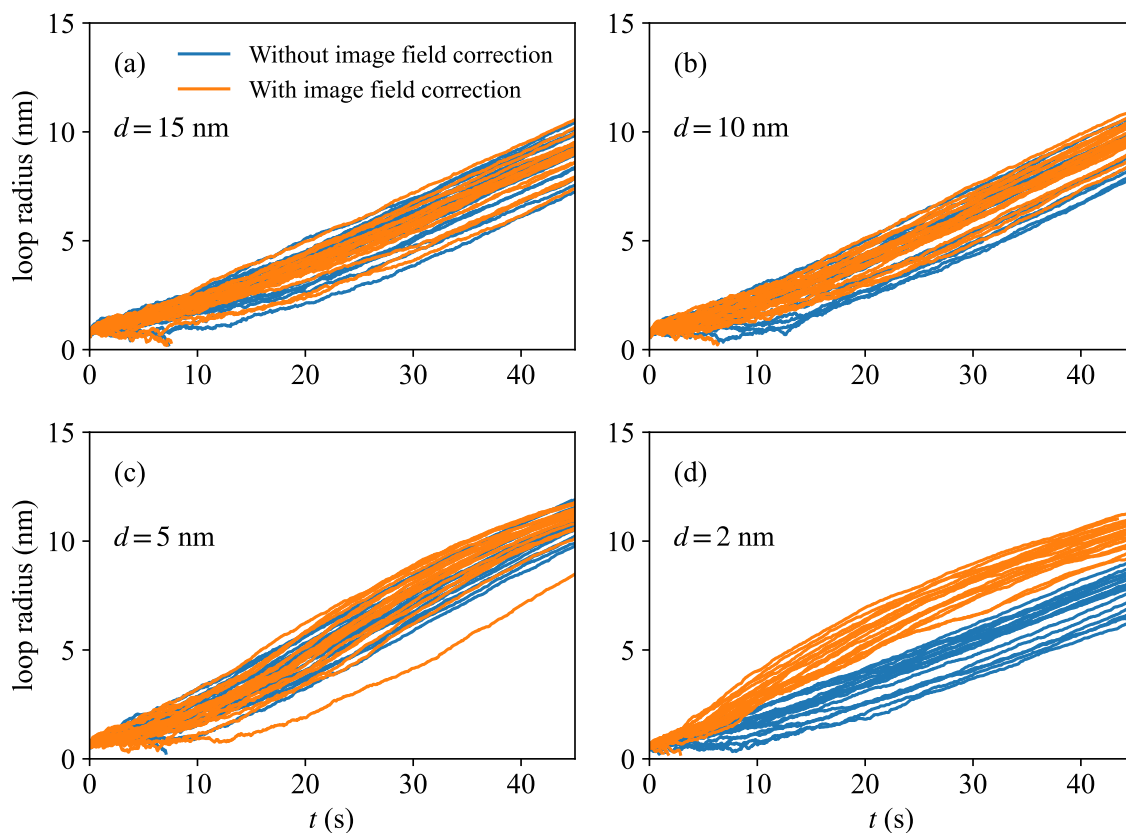


Figure 8. Evolution of loop radius with time for different distances to the surface d . 20 simulations have been performed for each value of d , with and without compensation of traction forces created by the elastic solution in an infinite medium.

531 4.3. Evolution of dislocation loops in thin foils under irradiation

532 It is known that in thin foils of fcc and bcc metals, interstitial dislocation loops
 533 grow under irradiation [62, 63]. This growth is explained successfully by the so-called
 534 “dislocation bias model” [2]. Loops interact more strongly with SIAs than vacancies,
 535 which results in a preferential absorption of SIAs. The remaining net quantity of
 536 vacancies in the matrix is absorbed by sinks which generate shorter range, or less
 537 intense, elastic fields. These sinks can be cavities, surfaces or grain boundaries for
 538 example. However, shrinkage of interstitial dislocation loops has been observed in some
 539 cases under irradiation. In aluminum, it has been documented by Jitsukawa and Hojou
 540 in 600 nm thick foils irradiated in a transmission electron microscope [64]. These authors
 541 have explained loop shrinkage by a dependency of the elastic bias of loops on their size.
 542 Indeed, even though all loops have a positive elastic bias, which means they interact
 543 more strongly with SIAs than vacancies, it does not imply that they all grow. Since
 544 vacancies and SIAs are produced in equal quantities, loops with the smallest elastic
 545 bias necessarily absorb more vacancies than SIAs if no sinks with lower elastic bias are
 546 present (for example, surfaces). In general, small loops tend to exhibit lower growth

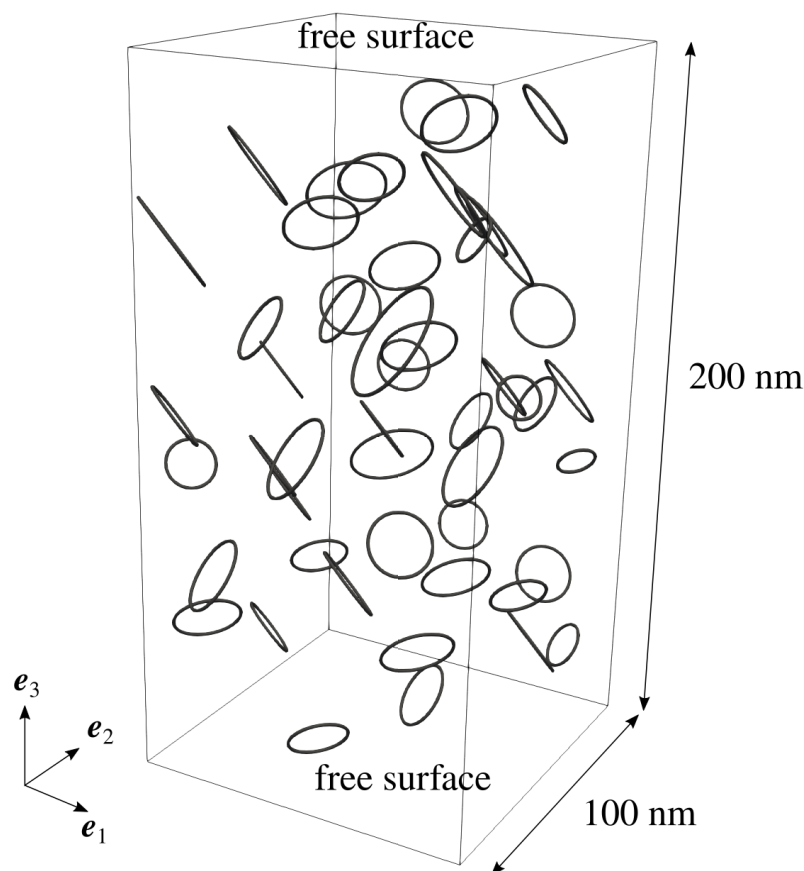


Figure 9. One of the 10 loop configurations considered to investigate loop growth dependency on distance to surface and loop radius.

547 rates than large loops, which points to an increase of the elastic bias with size. Numerical
 548 evaluations of bias of isolated loops are consistent with these findings [65, 66, 67].

549 Absorption efficiencies of loops depend not only on their size, but also on the
 550 surrounding microstructure [17, 16]. To assess more precisely the effect of elastic bias
 551 on loop behaviour, we simulate microstructures containing several loops of various sizes.
 552 We consider a system of size $100 \text{ nm} \times 100 \text{ nm} \times 200 \text{ nm}$, with free surfaces along e_3
 553 and PBCs in the two other directions. 50 dislocation loops are randomly placed in
 554 the simulation box, which represents a loop density of $2.5 \times 10^{22} \text{ m}^{-3}$. Their radius is
 555 drawn from a normal distribution of mean 10 nm and of standard deviation 2 nm, and
 556 their habit plane is chosen randomly among the four possible ones. A total of 10 loop
 557 configurations are generated. Each configuration is simulated 5 times, with different
 558 random seeds, and the average growth rate of a loop is deduced from linear fits of the
 559 evolution of loop radius over 10 seconds. SIAs and vacancies are produced as Frenkel
 560 pairs, at a dose rate of 10^{-4} dpa/s . An example of a loop microstructure is shown
 561 in Fig. 9. No other sinks, such as cavities or grain boundaries, are introduced in the
 562 simulation.

563 Loop growth rate has a clear dependency on the distance of the loop to the surface
564 d (Fig. 10-(a)). On average, loops close to the surface have the highest growth rate,
565 because vacancies can easily reach the surface. For values of d larger than around 40 nm,
566 surface effects become negligible. Vacancies are mostly absorbed by loops, which results
567 in slow growth and even shrinkage of loops. The growth rate is plotted as a function
568 of the loop radius in Fig. 10-(b), for loops which are more than 40 nm away from both
569 surfaces. On average, the growth rate increases with the loop radius, although values are
570 very scattered. This result is consistent with experiments and with the bias calculations
571 on isolated loops, which show a strong increase of bias for small radii and a plateau
572 at around 10 nm [66, 67]. The large scattering of growth rates points to an additional
573 effect of the surrounding microstructure on the loop behaviour. Recently, it has been
574 shown that to first order, the absorption efficiency of a loop is proportional to $(V/\bar{V})^{1/4}$,
575 where V is the Voronoi volume of the loop and \bar{V} is the average Voronoi volume [16].
576 The growth rate also seems to follow this trend (Fig. 10-(c)). The scattering is however
577 large, which highlights the complex dependency of loop growth rate on the surrounding
578 microstructure, especially when long range elastic interactions are taken into account.
579 If other microstructural features with lower elastic bias, such as cavities, are present in
580 sufficient number in the bulk, loop growth rates are expected to become all positive but
581 still scattered.

582 Conclusion

583 A method has been proposed to efficiently and accurately estimate the strain field
584 generated by defects in irradiated microstructures, in the framework of OKMC
585 simulations. The strain field of cavities and dislocation segments is evaluated by a local
586 expansion in spherical harmonics if the sources are sufficiently far from the evaluation
587 point. Otherwise, a direct sum over the strain sources is performed. This leads to a
588 drastic reduction in the evaluation time of the field compared to a direct summation
589 over strain sources, especially if periodic boundary conditions are used.

590 To evaluate efficiently the local expansion coefficients, the FMM for biharmonic
591 kernels, which relies on two calls to FMM for harmonic kernels, is used. The number
592 of FMM calls is reduced with respect to previous approaches and kept independent on
593 the number of field types (cavities, dislocation segments). These improvements could
594 be interesting for other simulation methods which rely on FMM on biharmonic kernels,
595 such as DDD.

596 In addition to its efficiency, another advantage of FMM is the relatively
597 straightforward treatment of finite systems. If surfaces are located far away in the
598 three directions of space and if the strain field contains a dipolar component, the sum of
599 strain contributions over periodic images is conditionally convergent. The correction to
600 this sum to give a system free from surface tractions is easily obtained from the multipole
601 expansion of the system, which is a by-product of FMM. This situation is quite common
602 in practice: it arises, for example, when the microstructure contains dislocation loops

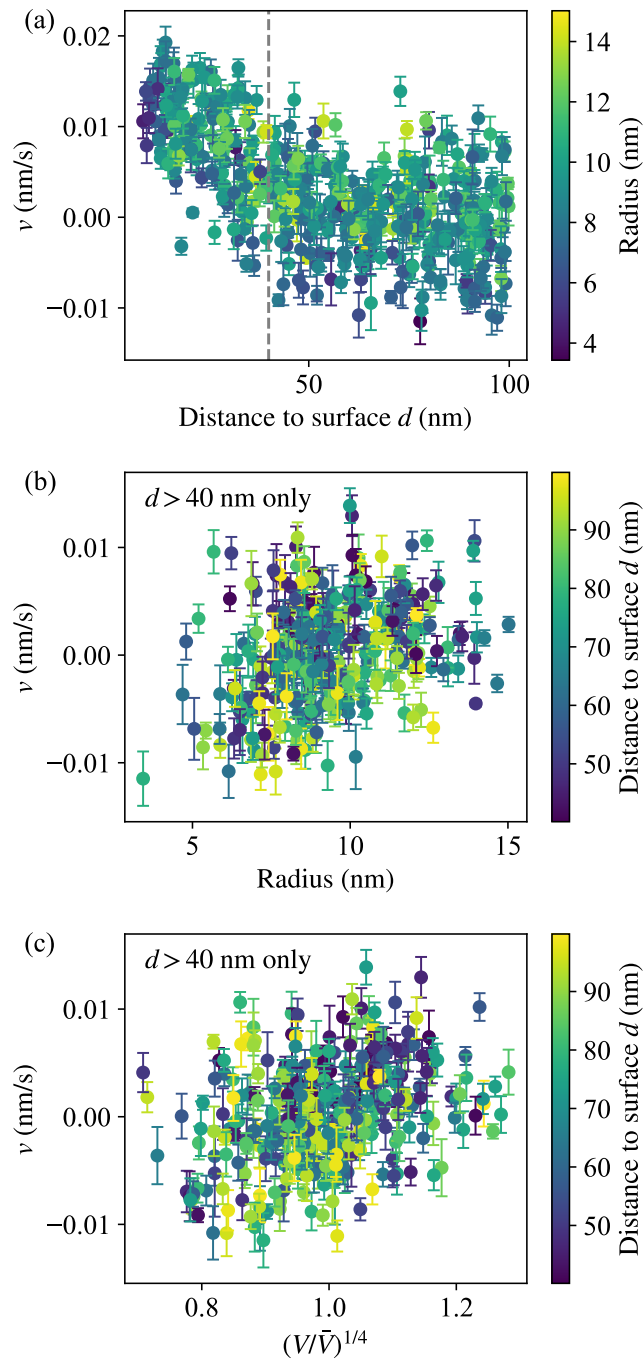


Figure 10. Loop growth rate in a 200 nm thick aluminum foil, irradiated at 10^{-4} dpa/s at 300 K. The system size is 100 nm in the two other directions. 10 loop configurations are simulated. Initial configurations contain a random arrangement of 50 loops, which corresponds to a density of $2.5 \times 10^{22} \text{ m}^{-3}$. The loop radius is chosen randomly from a gaussian distribution of mean value 10 nm and of standard deviation 2 nm. Error bars correspond to the standard error of the mean calculated on 5 independent simulations of the same configuration. (a) Loop growth rate as a function of the distance of the loop to the closest surface d . (b) Loop growth rate as a function of the loop radius. Only loops which are more than 40 nm away from both surfaces are shown. (c) Loop growth rate as a function of $(V/\bar{V})^{1/4}$, where V is the Voronoi volume of the loop and \bar{V} is the average Voronoi volume.

603 and cavities. If some surfaces correspond to the boundaries of the simulation box, an
 604 elastic problem with prescribed tractions on some of the boundaries must be solved with
 605 FEM. The adaptive mesh of the FMM is particularly convenient to build a FEM mesh
 606 fitting the variations of traction forces.

607 Preliminary simulations of loop microstructures with elastic interactions reveal the
 608 large scattering of loop growth rates, although correlations with loop radius and with
 609 the Voronoi volume of loops have been highlighted. These results show that using elastic
 610 bias of isolated defects is probably not sufficient to provide a quantitative description
 611 of irradiated microstructures.

612 Acknowledgments

613 This work has been carried out partly within the framework of the EUROfusion
 614 Consortium and has received funding from the Euratom research and training program
 615 under grant agreements No 633053 and 101052200 – EUROfusion. Views and opinions
 616 expressed are however those of the author only and do not necessarily reflect those of
 617 the European Union or the European Commission. Neither the European Union nor
 618 the European Commission can be held responsible for them.

619 Appendix A. Strain components for a dislocation loop

Using the notations from Section 1.2.1, explicit expressions of the strain components for
 a dislocation loop are (the dependency on v_α is dropped for clarity):

$$\begin{aligned} \varepsilon_{11}(\bar{\mathbf{x}}) = & \frac{1}{8\pi} \sum_{\alpha=1}^{N_q} w_\alpha \left[\frac{1}{1-\nu} (b_3\bar{x}_{,112} - b_2\bar{x}_{,113}) x'_{1,v} \right. \\ & + \left(\frac{\nu}{1-\nu} b_1\bar{x}_{,113} - b_1\bar{x}_{,223} - b_1\bar{x}_{,333} - \frac{\nu}{1-\nu} b_3\bar{x}_{,111} + b_3\bar{x}_{,221} + b_3\bar{x}_{,331} \right) x'_{2,v} \\ & \left. + \left(-\frac{\nu}{1-\nu} b_1\bar{x}_{,112} + b_1\bar{x}_{,222} + b_1\bar{x}_{,332} + \frac{\nu}{1-\nu} b_2\bar{x}_{,111} - b_2\bar{x}_{,221} - b_2\bar{x}_{,331} \right) x'_{3,v} \right] \quad (\text{A.1}) \end{aligned}$$

$$\begin{aligned} \varepsilon_{22}(\bar{\mathbf{x}}) = & \frac{1}{8\pi} \sum_{\alpha=1}^{N_q} w_\alpha \left[\left(-\frac{\nu}{1-\nu} b_2\bar{x}_{,223} + b_2\bar{x}_{,333} + b_2\bar{x}_{,113} + \frac{\nu}{1-\nu} b_3\bar{x}_{,222} - b_3\bar{x}_{,332} - b_3\bar{x}_{,112} \right) x'_{1,v} \right. \\ & + \frac{1}{1-\nu} (b_1\bar{x}_{,223} - b_3\bar{x}_{,221}) x'_{2,v} \\ & \left. + \left(\frac{\nu}{1-\nu} b_2\bar{x}_{,211} - b_2\bar{x}_{,331} - b_2\bar{x}_{,111} - \frac{\nu}{1-\nu} b_1\bar{x}_{,222} + b_1\bar{x}_{,332} + b_1\bar{x}_{,112} \right) x'_{3,v} \right] \quad (\text{A.2}) \end{aligned}$$

$$\begin{aligned} \varepsilon_{33}(\bar{\mathbf{x}}) = & \frac{1}{8\pi} \sum_{\alpha=1}^{N_q} w_{\alpha} \left[\left(\frac{\nu}{1-\nu} b_3 \bar{x}_{,332} - b_3 \bar{x}_{,112} - b_3 \bar{x}_{,222} - \frac{\nu}{1-\nu} b_2 \bar{x}_{,333} + b_2 \bar{x}_{,113} + b_2 \bar{x}_{,223} \right) x'_{1,v} \right. \\ & + \left(-\frac{\nu}{1-\nu} b_3 \bar{x}_{,331} + b_3 \bar{x}_{,111} + b_3 \bar{x}_{,221} + \frac{\nu}{1-\nu} b_1 \bar{x}_{,333} - b_1 \bar{x}_{,113} - b_1 \bar{x}_{,223} \right) x'_{2,v} \\ & \left. + \frac{1}{1-\nu} (b_2 \bar{x}_{,331} - b_1 \bar{x}_{,332}) x'_{3,v} \right] \quad (\text{A.3}) \end{aligned}$$

$$\begin{aligned} \varepsilon_{23}(\bar{\mathbf{x}}) = & \frac{1}{8\pi} \sum_{\alpha=1}^{N_q} w_{\alpha} \left[\frac{1}{1-\nu} (b_3 \bar{x}_{,223} - b_2 \bar{x}_{,332}) x'_{1,v} \right. \\ & + \frac{1}{2} \left(b_2 \bar{x}_{,111} + b_2 \bar{x}_{,221} + b_2 \bar{x}_{,331} - b_1 \bar{x}_{,112} - b_1 \bar{x}_{,222} + \frac{1+\nu}{1-\nu} b_1 \bar{x}_{,332} - \frac{2}{1-\nu} b_3 \bar{x}_{,123} \right) x'_{2,v} \\ & \left. + \frac{1}{2} \left(-b_3 \bar{x}_{,111} - b_3 \bar{x}_{,221} - b_3 \bar{x}_{,331} + b_1 \bar{x}_{,113} - \frac{1+\nu}{1-\nu} b_1 \bar{x}_{,223} + b_1 \bar{x}_{,333} + \frac{2}{1-\nu} b_2 \bar{x}_{,123} \right) x'_{3,v} \right] \quad (\text{A.4}) \end{aligned}$$

$$\begin{aligned} \varepsilon_{13}(\bar{\mathbf{x}}) = & \frac{1}{8\pi} \sum_{\alpha=1}^{N_q} w_{\alpha} \left[\frac{1}{2} \left(-b_1 \bar{x}_{,222} - b_1 \bar{x}_{,332} - b_1 \bar{x}_{,112} + b_2 \bar{x}_{,221} - \frac{1+\nu}{1-\nu} b_2 \bar{x}_{,331} + b_2 \bar{x}_{,111} + \frac{2}{1-\nu} b_3 \bar{x}_{,123} \right) x'_{1,v} \right. \\ & + \frac{1}{1-\nu} (b_1 \bar{x}_{,331} - b_3 \bar{x}_{,113}) x'_{2,v} \\ & \left. + \frac{1}{2} \left(b_3 \bar{x}_{,222} + b_3 \bar{x}_{,332} + b_3 \bar{x}_{,112} - b_2 \bar{x}_{,223} - b_2 \bar{x}_{,333} + \frac{1+\nu}{1-\nu} b_2 \bar{x}_{,113} - \frac{2}{1-\nu} b_1 \bar{x}_{,123} \right) x'_{3,v} \right] \quad (\text{A.5}) \end{aligned}$$

$$\begin{aligned} \varepsilon_{12}(\bar{\mathbf{x}}) = & \frac{1}{8\pi} \sum_{\alpha=1}^{N_q} w_{\alpha} \left[\frac{1}{2} \left(b_1 \bar{x}_{,333} + b_1 \bar{x}_{,113} + b_1 \bar{x}_{,223} - b_3 \bar{x}_{,331} - b_3 \bar{x}_{,111} + \frac{1+\nu}{1-\nu} b_3 \bar{x}_{,221} - \frac{2}{1-\nu} b_2 \bar{x}_{,123} \right) x'_{1,v} \right. \\ & + \frac{1}{2} \left(-b_2 \bar{x}_{,333} - b_2 \bar{x}_{,113} - b_2 \bar{x}_{,223} + b_3 \bar{x}_{,332} - \frac{1+\nu}{1-\nu} b_3 \bar{x}_{,112} + b_3 \bar{x}_{,222} + \frac{2}{1-\nu} b_1 \bar{x}_{,123} \right) x'_{2,v} \\ & \left. + \frac{1}{1-\nu} (b_2 \bar{x}_{,112} - b_1 \bar{x}_{,221}) x'_{3,v} \right]. \quad (\text{A.6}) \end{aligned}$$

620 Expressions of $\bar{x}_{,ijk}$ are given, for example, in Ref. [34].

621 Appendix B. Definition of spherical harmonics, solid harmonics and 622 recursion formulas

623 The definition of spherical harmonics used here is the same as in Ref. [24]:

$$Y_l^m(\theta, \varphi) = \sqrt{\frac{(l-|m|)!}{(l+|m|)!}} P_l^{|m|}(\cos \theta) e^{im\varphi}, \quad (\text{B.1})$$

624 where P_l^m are the associated Legendre polynomials, which are defined by

$$P_l^m(x) = (-1)^m (1-x^2)^{m/2} \frac{d^m}{dx^m} P_l(x). \quad (\text{B.2})$$

625 In Eq. (B.2), P_l are the Legendre polynomials. From Eq. (B.1) we deduce that
626 $(Y_l^m(\theta, \varphi))^* = Y_l^{-m}(\theta, \varphi)$. The normalisation is such that

$$\int_0^{2\pi} \int_0^\pi Y_l^m(\theta, \varphi) (Y_{l'}^{m'}(\theta, \varphi))^* \sin \theta \, d\theta \, d\varphi = \frac{4\pi}{2l+1} \delta_{ll'} \delta_{mm'}. \quad (\text{B.3})$$

627 For example we have:

$$Y_1^0(\theta, \varphi) = \cos \theta \quad (\text{B.4})$$

$$Y_1^1(\theta, \varphi) = -\frac{1}{\sqrt{2}} \sin \theta e^{i\varphi}. \quad (\text{B.5})$$

628 Regular solid harmonics are defined by $R_l^m(x, \theta, \varphi) = x^l Y_l^m(\theta, \varphi)$ and irregular solid
629 harmonics are defined by $I_l^m(x, \theta, \varphi) = Y_l^m(\theta, \varphi)/x^{l+1}$. Irregular solid harmonics can also
630 be written as [68, 27]

$$I_l^m(x, \theta, \varphi) = (-1)^m A_l^m \left(\frac{\partial}{\partial x_1} + i \frac{\partial}{\partial x_2} \right)^m \left(\frac{\partial}{\partial x_3} \right)^{l-m} \left(\frac{1}{x} \right), \quad (\text{B.6})$$

631 with

$$A_l^m = \frac{(-1)^l}{\sqrt{(l-m)!(l+m)!}} \quad (\text{B.7})$$

632 (the factor $(-1)^m$ in Eq. (B.6) is missing in [27]).

633 We note

$$B_l^m = \sqrt{(l+m)(l-m)}, \quad (\text{B.8})$$

634

$$C_l^m = \sqrt{(l+m)(l+m-1)}, \quad (\text{B.9})$$

635 and

$$s(m) = \begin{cases} 1 & \text{if } m \geq 0 \\ -1 & \text{if } m < 0. \end{cases} \quad (\text{B.10})$$

636 We can write recursion formulas under the form:

$$B_{l+1}^m Y_{l+1}^m - (2l+1) Y_1^0 Y_l^m + B_l^m Y_{l-1}^m = 0 \quad (\text{B.11})$$

$$s(m-1) C_{l+1}^{-m+1} Y_{l+1}^{m-1} + \sqrt{2}(2l+1) Y_1^{-1} Y_l^m - s(m-1) C_l^m Y_{l-1}^{m-1} = 0 \quad (\text{B.12})$$

$$s(m) C_{l+2}^m Y_{l+1}^{m+1} - \sqrt{2}(2l+1) Y_1^1 Y_l^m - s(m) C_l^{-m} Y_{l-1}^{m+1} = 0. \quad (\text{B.13})$$

637 Using these formulas, it can be shown that products $x_k I_l^m(x, \theta, \varphi)$ can be
 638 decomposed as functions of $I_p^q(x, \theta, \varphi)$ and $x^2 I_p^q(x, \theta, \varphi)$:

$$\begin{aligned}
 x_1 I_l^m(x, \theta, \varphi) = & -\frac{1}{2(2l+1)} s(m) C_{l+2}^m x^2 I_{l+1}^{m+1}(x, \theta, \varphi) \\
 & + \frac{1}{2(2l+1)} s(m-1) C_{l+1}^{-m+1} x^2 I_{l+1}^{m-1}(x, \theta, \varphi) \\
 & + \frac{1}{2(2l+1)} s(m) C_l^{-m} I_{l-1}^{m+1}(x, \theta, \varphi) \\
 & - \frac{1}{2(2l+1)} s(m-1) C_l^m I_{l-1}^{m-1}(x, \theta, \varphi) \quad (\text{B.14})
 \end{aligned}$$

639

$$\begin{aligned}
 x_2 I_l^m(x, \theta, \varphi) = & \frac{i}{2(2l+1)} s(m-1) C_{l+1}^{-m+1} x^2 I_{l+1}^{m-1}(x, \theta, \varphi) \\
 & + \frac{i}{2(2l+1)} s(m) C_{l+2}^m x^2 I_{l+1}^{m+1}(x, \theta, \varphi) \\
 & - \frac{i}{2(2l+1)} s(m) C_l^{-m} I_{l-1}^{m+1}(x, \theta, \varphi) \\
 & - \frac{i}{2(2l+1)} s(m-1) C_l^m I_{l-1}^{m-1}(x, \theta, \varphi) \quad (\text{B.15})
 \end{aligned}$$

640

$$x_3 I_l^m(x, \theta, \varphi) = \frac{B_{l+1}^m}{2l+1} x^2 I_{l+1}^m(x, \theta, \varphi) + \frac{B_l^m}{2l+1} I_{l-1}^m(x, \theta, \varphi). \quad (\text{B.16})$$

641 Similar expressions can be deduced for $x_k R_l^m(x, \theta, \varphi)$, using Eqs (B.14)–(B.16) and
 642 the relation $R_l^m(x, \theta, \varphi) = x^{2l+1} I_l^m(x, \theta, \varphi)$:

$$\begin{aligned}
 x_1 R_l^m(x, \theta, \varphi) = & -\frac{1}{2(2l+1)} s(m) C_{l+2}^m R_{l+1}^{m+1}(x, \theta, \varphi) \\
 & + \frac{1}{2(2l+1)} s(m-1) C_{l+1}^{-m+1} R_{l+1}^{m-1}(x, \theta, \varphi) \\
 & + \frac{1}{2(2l+1)} s(m) C_l^{-m} x^2 R_{l-1}^{m+1}(x, \theta, \varphi) \\
 & - \frac{1}{2(2l+1)} s(m-1) C_l^m x^2 R_{l-1}^{m-1}(x, \theta, \varphi) \quad (\text{B.17})
 \end{aligned}$$

643

$$\begin{aligned}
 x_2 R_l^m(x, \theta, \varphi) = & \frac{i}{2(2l+1)} s(m) C_{l+2}^m R_{l+1}^{m+1}(x, \theta, \varphi) \\
 & + \frac{i}{2(2l+1)} s(m-1) C_{l+1}^{-m+1} R_{l+1}^{m-1}(x, \theta, \varphi) \\
 & - \frac{i}{2(2l+1)} s(m) C_l^{-m} x^2 R_{l-1}^{m+1}(x, \theta, \varphi) \\
 & - \frac{i}{2(2l+1)} s(m-1) C_l^m x^2 R_{l-1}^{m-1}(x, \theta, \varphi) \quad (\text{B.18})
 \end{aligned}$$

644

$$x_3 R_l^m(x, \theta, \varphi) = \frac{B_{l+1}^m}{2l+1} R_{l+1}^m(x, \theta, \varphi) + \frac{B_l^m}{2l+1} x^2 R_{l-1}^m(x, \theta, \varphi). \quad (\text{B.19})$$

645 **Appendix C. Translation and conversion of expansions for a biharmonic**
 646 **function**

647 In this section the results of Gumerov and Duraiswami [39] are given for our definition
 648 of spherical harmonics. Let $\psi(\mathbf{x}) = \phi(\mathbf{x}) + x^2\omega(\mathbf{x})$ be a multipole or local expansion of
 649 a biharmonic function. We want to set the origin of the expansion at \mathbf{t} , *i.e.* we consider
 650 the new function (Fig. C1)

$$\begin{aligned}\hat{\psi}(\mathbf{x}) &= \psi(\mathbf{x} + \mathbf{t}) \\ &= \phi(\mathbf{x} + \mathbf{t}) + (\mathbf{x} + \mathbf{t}) \cdot (\mathbf{x} + \mathbf{t})\omega(\mathbf{x} + \mathbf{t}) \\ &= \hat{\phi}(\mathbf{x}) + (x^2 + 2\mathbf{x} \cdot \mathbf{t} + t^2)\hat{\omega}(\mathbf{x}),\end{aligned}\tag{C.1}$$

651 where $\hat{\phi}$ and $\hat{\omega}$ are the same expansions as ϕ and ω , but with their origin at \mathbf{t} , *i.e.*
 652 their coefficients are deduced from the expansions ϕ and ω by translation or conversion
 653 operators of harmonic functions [24, 25]. We want to set Eq. (C.1) under the form

$$\hat{\psi}(\mathbf{x}) = \tilde{\phi}(\mathbf{x}) + x^2\tilde{\omega}(\mathbf{x}),\tag{C.2}$$

654 where $\tilde{\phi}$ and $\tilde{\omega}$ remain to be found. Operators which transform the coefficients
 655 of the expansion (ϕ, ω) into the coefficients of the expansion $(\tilde{\phi}, \tilde{\omega})$ are the
 656 translation/conversion operators which are used in the FMM.

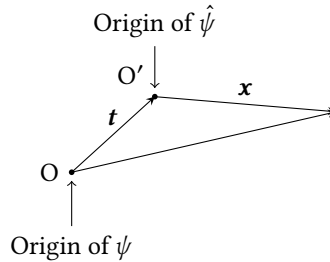


Figure C1. Change of center of expansion.

657 Two cases can be distinguished:

- 658 • For a multipole-to-multipole (M2M) transformation (translation), $\hat{\phi}(\mathbf{x})$ and $\hat{\omega}(\mathbf{x})$
 659 are expanded with irregular solid harmonics. Eqs (B.14)–(B.16) can be used to
 660 write the term $2\mathbf{x} \cdot \mathbf{t}\hat{\omega}(\mathbf{x})$ as contributions to $\tilde{\phi}(\mathbf{x})$ and $\tilde{\omega}(\mathbf{x})$. We obtain

$$\tilde{\phi}_l^m = \hat{\phi}_l^m + t^2\hat{\omega}_l^m - \hat{\omega}_{l+1}^{m+1}\frac{t_1 + it_2}{2l + 3}s(m)C_{l+1}^{m+1} + \hat{\omega}_{l+1}^m\frac{2t_3}{2l + 3}B_{l+1}^m + \hat{\omega}_{l+1}^{m-1}\frac{t_1 - it_2}{2l + 3}s(m-1)C_{l+1}^{-m+1}\tag{C.3}$$

$$\tilde{\omega}_l^m = \hat{\omega}_l^m + \hat{\omega}_{l-1}^{m+1}\frac{t_1 + it_2}{2l - 1}s(m)C_l^{-m} + \hat{\omega}_{l-1}^m\frac{2t_3}{2l - 1}B_l^m - \hat{\omega}_{l-1}^{m-1}\frac{t_1 - it_2}{2l - 1}s(m-1)C_{l+1}^{m-1}.\tag{C.4}$$

661 These expressions correspond to expression 57 in Ref. [39] obtained with a different
 662 definition of spherical harmonics.

- 663 • For a multipole-to-local (M2L) or a local-to-local (L2L) transformation, $\hat{\phi}(\mathbf{x})$ and
 664 $\hat{\omega}(\mathbf{x})$ are expanded with regular solid harmonics. Eqs (B.17)–(B.19) can be used to
 665 write the term $2\mathbf{x} \cdot \mathbf{t}\hat{\omega}(\mathbf{x})$ as contributions to $\tilde{\phi}(\mathbf{x})$ and $\tilde{\omega}(\mathbf{x})$. We obtain

$$\tilde{\phi}_l^m = \hat{\phi}_l^m + t^2 \hat{\omega}_l^m + \hat{\omega}_{l-1}^{m+1} \frac{t_1 + it_2}{2l-1} s(m) C_l^{-m} + \hat{\omega}_{l-1}^m \frac{2t_3}{2l-1} B_l^m - \hat{\omega}_{l-1}^{m-1} \frac{t_1 - it_2}{2l-1} s(m-1) C_{l+1}^{m-1} \quad (\text{C.5})$$

$$\tilde{\omega}_l^m = \hat{\omega}_l^m - \hat{\omega}_{l+1}^{m+1} \frac{t_1 + it_2}{2l+3} s(m) C_{l+1}^{m+1} + \hat{\omega}_{l+1}^m \frac{2t_3}{2l+3} B_{l+1}^m + \hat{\omega}_{l+1}^{m-1} \frac{t_1 - it_2}{2l+3} s(m-1) C_{l+1}^{-m+1}. \quad (\text{C.6})$$

666 These expressions correspond to expression 56 in Ref. [39].

667 Appendix D. Derivatives of irregular solid harmonics

668 Derivatives of irregular solid harmonics are used in the local expansion of the strain field
 669 of a cavity (Eq. (25)) and a dislocation segment (Eqs (32)–(33)). They are also used
 670 to obtain the derivatives of regular solid harmonics (Appendix E). To determine them,
 671 it is convenient to use expression (B.6). The dependency of I_l^m functions on x, θ, φ is
 672 dropped for clarity.

673 First derivatives

- $m = 0$

$$\frac{\partial}{\partial x_1}(I_l^0) = \frac{1}{2} \sqrt{(l+1)(l+2)}(I_{l+1}^1 + I_{l+1}^{-1}) \quad (\text{D.1})$$

$$\frac{\partial}{\partial x_2}(I_l^0) = -\frac{i}{2} \sqrt{(l+1)(l+2)}(I_{l+1}^1 - I_{l+1}^{-1}) \quad (\text{D.2})$$

$$\frac{\partial}{\partial x_3}(I_l^0) = -(l+1)I_{l+1}^0 \quad (\text{D.3})$$

- $m \geq 1$

$$\frac{\partial}{\partial x_1}(I_l^m) = \frac{1}{2} \left(\sqrt{(l+m+2)(l+m+1)} I_{l+1}^{m+1} - \sqrt{(l-m+2)(l-m+1)} I_{l+1}^{m-1} \right) \quad (\text{D.4})$$

$$\frac{\partial}{\partial x_2}(I_l^m) = -\frac{i}{2} \left(\sqrt{(l+m+2)(l+m+1)} I_{l+1}^{m+1} + \sqrt{(l-m+2)(l-m+1)} I_{l+1}^{m-1} \right) \quad (\text{D.5})$$

$$\frac{\partial}{\partial x_3}(I_l^m) = -\sqrt{(l+m+1)(l-m+1)} I_{l+1}^m \quad (\text{D.6})$$

674 Second derivatives

- $m = 0$

$$\begin{aligned} \frac{\partial^2}{\partial x_1^2}(I_l^0) &= \frac{1}{4} \sqrt{(l+1)(l+2)(l+3)(l+4)} I_{l+2}^2 - \frac{1}{2} (l+1)(l+2) I_{l+2}^0 \\ &\quad + \frac{1}{4} \sqrt{(l+1)(l+2)(l+3)(l+4)} I_{l+2}^{-2} \quad (\text{D.7}) \end{aligned}$$

$$\begin{aligned} \frac{\partial^2}{\partial x_2^2}(I_l^0) = & -\frac{1}{4}\sqrt{(l+1)(l+2)(l+3)(l+4)}I_{l+2}^2 - \frac{1}{2}(l+1)(l+2)I_{l+2}^0 \\ & - \frac{1}{4}\sqrt{(l+1)(l+2)(l+3)(l+4)}I_{l+2}^{-2} \end{aligned} \quad (\text{D.8})$$

$$\frac{\partial^2}{\partial x_3^2}(I_l^0) = (l+1)(l+2)I_{l+2}^0 \quad (\text{D.9})$$

$$\begin{aligned} \frac{\partial^2}{\partial x_1 \partial x_2}(I_l^0) = & -\frac{i}{4}\sqrt{(l+1)(l+2)(l+3)(l+4)}I_{l+2}^2 \\ & + \frac{i}{4}\sqrt{(l+1)(l+2)(l+3)(l+4)}I_{l+2}^{-2} \end{aligned} \quad (\text{D.10})$$

$$\frac{\partial^2}{\partial x_2 \partial x_3}(I_l^0) = \frac{i}{2}(l+1)\sqrt{(l+2)(l+3)}(I_{l+2}^1 - I_{l+2}^{-1}) \quad (\text{D.11})$$

$$\frac{\partial^2}{\partial x_1 \partial x_3}(I_l^0) = -\frac{1}{2}(l+1)\sqrt{(l+2)(l+3)}(I_{l+2}^1 + I_{l+2}^{-1}) \quad (\text{D.12})$$

- $m = 1$

$$\begin{aligned} \frac{\partial^2}{\partial x_1^2}(I_l^1) = & \frac{1}{4}\sqrt{(l+2)(l+3)(l+4)(l+5)}I_{l+2}^3 - \frac{1}{2}\sqrt{l(l+1)(l+2)(l+3)}I_{l+2}^1 \\ & - \frac{1}{4}\sqrt{l(l+1)(l+2)(l+3)}I_{l+2}^{-1} \end{aligned} \quad (\text{D.13})$$

$$\begin{aligned} \frac{\partial^2}{\partial x_2^2}(I_l^1) = & -\frac{1}{4}\sqrt{(l+2)(l+3)(l+4)(l+5)}I_{l+2}^3 - \frac{1}{2}\sqrt{l(l+1)(l+2)(l+3)}I_{l+2}^1 \\ & + \frac{1}{4}\sqrt{l(l+1)(l+2)(l+3)}I_{l+2}^{-1} \end{aligned} \quad (\text{D.14})$$

$$\frac{\partial^2}{\partial x_3^2}(I_l^1) = \sqrt{l(l+1)(l+2)(l+3)}I_{l+2}^1 \quad (\text{D.15})$$

$$\begin{aligned} \frac{\partial^2}{\partial x_1 \partial x_2}(I_l^1) = & -\frac{i}{4}\sqrt{(l+2)(l+3)(l+4)(l+5)}I_{l+2}^3 \\ & - \frac{i}{4}\sqrt{l(l+1)(l+2)(l+3)}I_{l+2}^{-1} \end{aligned} \quad (\text{D.16})$$

$$\frac{\partial^2}{\partial x_2 \partial x_3}(I_l^1) = \frac{i}{2}\sqrt{l(l+2)(l+3)(l+4)}I_{l+2}^2 + \frac{i}{2}(l+2)\sqrt{l(l+1)}I_{l+2}^0 \quad (\text{D.17})$$

$$\frac{\partial^2}{\partial x_1 \partial x_3}(I_l^1) = -\frac{1}{2}\sqrt{l(l+2)(l+3)(l+4)}I_{l+2}^2 + \frac{1}{2}(l+2)\sqrt{l(l+1)}I_{l+2}^0 \quad (\text{D.18})$$

- $m \geq 2$

$$\begin{aligned} \frac{\partial^2}{\partial x_1^2}(I_l^m) &= \frac{1}{4}\sqrt{(l+m+1)(l+m+2)(l+m+3)(l+m+4)}I_{l+2}^{m+2} \\ &\quad - \frac{1}{2}\sqrt{(l-m+2)(l-m+1)(l+m+1)(l+m+2)}I_{l+2}^m \\ &\quad + \frac{1}{4}\sqrt{(l-m+1)(l-m+2)(l-m+3)(l-m+4)}I_{l+2}^{m-2} \end{aligned} \quad (\text{D.19})$$

$$\begin{aligned} \frac{\partial^2}{\partial x_2^2}(I_l^m) &= -\frac{1}{4}\sqrt{(l+m+1)(l+m+2)(l+m+3)(l+m+4)}I_{l+2}^{m+2} \\ &\quad - \frac{1}{2}\sqrt{(l-m+1)(l-m+2)(l+m+1)(l+m+2)}I_{l+2}^m \\ &\quad - \frac{1}{4}\sqrt{(l-m+1)(l-m+2)(l-m+3)(l-m+4)}I_{l+2}^{m-2} \end{aligned} \quad (\text{D.20})$$

$$\frac{\partial^2}{\partial x_3^2}(I_l^m) = \sqrt{(l-m+1)(l-m+2)(l+m+1)(l+m+2)}I_{l+2}^m \quad (\text{D.21})$$

$$\begin{aligned} \frac{\partial^2}{\partial x_1 \partial x_2}(I_l^m) &= -\frac{i}{4}\sqrt{(l+m+1)(l+m+2)(l+m+3)(l+m+4)}I_{l+2}^{m+2} \\ &\quad + \frac{i}{4}\sqrt{(l-m+1)(l-m+2)(l-m+3)(l-m+4)}I_{l+2}^{m-2} \end{aligned} \quad (\text{D.22})$$

$$\begin{aligned} \frac{\partial^2}{\partial x_2 \partial x_3}(I_l^m) &= \frac{i}{2}\sqrt{(l-m+1)(l+m+1)(l+m+2)(l+m+3)}I_{l+2}^{m+1} \\ &\quad + \frac{i}{2}\sqrt{(l-m+1)(l-m+2)(l-m+3)(l+m+1)}I_{l+2}^{m-1} \end{aligned} \quad (\text{D.23})$$

$$\begin{aligned} \frac{\partial^2}{\partial x_1 \partial x_3}(I_l^m) &= -\frac{1}{2}\sqrt{(l-m+1)(l+m+1)(l+m+2)(l+m+3)}I_{l+2}^{m+1} \\ &\quad + \frac{1}{2}\sqrt{(l-m+1)(l-m+2)(l-m+3)(l+m+1)}I_{l+2}^{m-1} \end{aligned} \quad (\text{D.24})$$

675 Third derivatives

- $m = 0$

$$\begin{aligned} \frac{\partial^3}{\partial x_1^3}(I_l^0) &= \frac{1}{8}\sqrt{(l+1)(l+2)(l+3)(l+4)(l+5)(l+6)}(I_{l+3}^3 + I_{l+3}^{-3}) \\ &\quad - \frac{3}{8}(l+1)(l+2)\sqrt{(l+3)(l+4)}(I_{l+3}^1 + I_{l+3}^{-1}) \end{aligned} \quad (\text{D.25})$$

$$\begin{aligned} \frac{\partial^3}{\partial x_2^3}(I_l^0) &= \frac{i}{8}\sqrt{(l+1)(l+2)(l+3)(l+4)(l+5)(l+6)}(I_{l+3}^3 - I_{l+3}^{-3}) \\ &\quad + \frac{3i}{8}(l+1)(l+2)\sqrt{(l+3)(l+4)}(I_{l+3}^1 - I_{l+3}^{-1}) \end{aligned} \quad (\text{D.26})$$

$$\frac{\partial^3}{\partial x_3^3}(I_l^0) = -(l+1)(l+2)(l+3)I_{l+3}^0 \quad (\text{D.27})$$

$$\begin{aligned} \frac{\partial^3}{\partial x_1^2 \partial x_2}(I_l^0) &= -\frac{i}{8} \sqrt{(l+1)(l+2)(l+3)(l+4)(l+5)(l+6)}(I_{l+3}^3 - I_{l+3}^{-3}) \\ &\quad + \frac{i}{8} (l+1)(l+2) \sqrt{(l+3)(l+4)}(I_{l+3}^1 - I_{l+3}^{-1}) \end{aligned} \quad (\text{D.28})$$

$$\begin{aligned} \frac{\partial^3}{\partial x_1^2 \partial x_3}(I_l^0) &= -\frac{1}{4} (l+1) \sqrt{(l+2)(l+3)(l+4)(l+5)}(I_{l+3}^2 + I_{l+3}^{-2}) \\ &\quad + \frac{1}{2} (l+1)(l+2)(l+3)I_{l+3}^0 \end{aligned} \quad (\text{D.29})$$

$$\begin{aligned} \frac{\partial^3}{\partial x_1 \partial x_2^2}(I_l^0) &= -\frac{1}{8} \sqrt{(l+1)(l+2)(l+3)(l+4)(l+5)(l+6)}(I_{l+3}^3 + I_{l+3}^{-3}) \\ &\quad - \frac{1}{8} (l+1)(l+2) \sqrt{(l+3)(l+4)}(I_{l+3}^1 + I_{l+3}^{-1}) \end{aligned} \quad (\text{D.30})$$

$$\begin{aligned} \frac{\partial^3}{\partial x_2^2 \partial x_3}(I_l^0) &= \frac{1}{4} (l+1) \sqrt{(l+2)(l+3)(l+4)(l+5)}(I_{l+3}^2 + I_{l+3}^{-2}) \\ &\quad + \frac{1}{2} (l+1)(l+2)(l+3)I_{l+3}^0 \end{aligned} \quad (\text{D.31})$$

$$\frac{\partial^3}{\partial x_1 \partial x_3^2}(I_l^0) = \frac{1}{2} (l+1)(l+2) \sqrt{(l+3)(l+4)}(I_{l+3}^1 + I_{l+3}^{-1}) \quad (\text{D.32})$$

$$\frac{\partial^3}{\partial x_2 \partial x_3^2}(I_l^0) = -\frac{i}{2} (l+1)(l+2) \sqrt{(l+3)(l+4)}(I_{l+3}^1 - I_{l+3}^{-1}) \quad (\text{D.33})$$

$$\frac{\partial^3}{\partial x_1 \partial x_2 \partial x_3}(I_l^0) = \frac{i}{4} (l+1) \sqrt{(l+2)(l+3)(l+4)(l+5)}(I_{l+3}^2 - I_{l+3}^{-2}) \quad (\text{D.34})$$

- $m = 1$

$$\begin{aligned} \frac{\partial^3}{\partial x_1^3}(I_l^1) &= \frac{1}{8} \sqrt{(l+2)(l+3)(l+4)(l+5)(l+6)(l+7)}I_{l+3}^4 \\ &\quad - \frac{3}{8} \sqrt{l(l+1)(l+2)(l+3)(l+4)(l+5)}I_{l+3}^2 \\ &\quad + \frac{3}{8} (l+2)(l+3) \sqrt{l(l+1)}I_{l+3}^0 \\ &\quad - \frac{1}{8} \sqrt{l(l+1)(l+2)(l+3)(l+4)(l+5)}I_{l+3}^{-2} \end{aligned} \quad (\text{D.35})$$

$$\begin{aligned}
\frac{\partial^3}{\partial x_2^3}(I_l^1) &= \frac{i}{8}\sqrt{(l+2)(l+3)(l+4)(l+5)(l+6)(l+7)}I_{l+3}^4 \\
&\quad + \frac{3i}{8}\sqrt{l(l+1)(l+2)(l+3)(l+4)(l+5)}I_{l+3}^2 \\
&\quad + \frac{3i}{8}(l+2)(l+3)\sqrt{l(l+1)}I_{l+3}^0 \\
&\quad + \frac{i}{8}\sqrt{l(l+1)(l+2)(l+3)(l+4)(l+5)}I_{l+3}^{-2} \quad (\text{D.36})
\end{aligned}$$

$$\frac{\partial^3}{\partial x_3^3}(I_l^1) = -(l+2)\sqrt{l(l+1)(l+3)(l+4)}I_{l+3}^1 \quad (\text{D.37})$$

$$\begin{aligned}
\frac{\partial^3}{\partial x_1^2 \partial x_2}(I_l^1) &= -\frac{i}{8}\sqrt{(l+2)(l+3)(l+4)(l+5)(l+6)(l+7)}I_{l+3}^4 \\
&\quad + \frac{i}{8}\sqrt{l(l+1)(l+2)(l+3)(l+4)(l+5)}I_{l+3}^2 \\
&\quad + \frac{i}{8}(l+2)(l+3)\sqrt{l(l+1)}I_{l+3}^0 \\
&\quad - \frac{i}{8}\sqrt{l(l+1)(l+2)(l+3)(l+4)(l+5)}I_{l+3}^{-2} \quad (\text{D.38})
\end{aligned}$$

$$\begin{aligned}
\frac{\partial^3}{\partial x_1^2 \partial x_3}(I_l^1) &= -\frac{1}{4}\sqrt{l(l+2)(l+3)(l+4)(l+5)(l+6)}I_{l+3}^3 \\
&\quad + \frac{1}{2}(l+2)\sqrt{l(l+1)(l+3)(l+4)}I_{l+3}^1 \\
&\quad + \frac{1}{4}(l+2)\sqrt{l(l+1)(l+3)(l+4)}I_{l+3}^{-1} \quad (\text{D.39})
\end{aligned}$$

$$\begin{aligned}
\frac{\partial^3}{\partial x_1 \partial x_2^2}(I_l^1) &= -\frac{1}{8}\sqrt{(l+2)(l+3)(l+4)(l+5)(l+6)(l+7)}I_{l+3}^4 \\
&\quad - \frac{1}{8}\sqrt{l(l+1)(l+2)(l+3)(l+4)(l+5)}I_{l+3}^2 \\
&\quad + \frac{1}{8}(l+2)(l+3)\sqrt{l(l+1)}I_{l+3}^0 \\
&\quad + \frac{1}{8}\sqrt{l(l+1)(l+2)(l+3)(l+4)(l+5)}I_{l+3}^{-2} \quad (\text{D.40})
\end{aligned}$$

$$\begin{aligned}
\frac{\partial^3}{\partial x_2^2 \partial x_3}(I_l^1) &= \frac{1}{4}\sqrt{l(l+2)(l+3)(l+4)(l+5)(l+6)}I_{l+3}^3 \\
&\quad + \frac{1}{2}(l+2)\sqrt{l(l+1)(l+3)(l+4)}I_{l+3}^1 \\
&\quad - \frac{1}{4}(l+2)\sqrt{l(l+1)(l+3)(l+4)}I_{l+3}^{-1} \quad (\text{D.41})
\end{aligned}$$

$$\begin{aligned} \frac{\partial^3}{\partial x_1 \partial x_3^2} (I_l^1) &= \frac{1}{2} \sqrt{l(l+1)(l+2)(l+3)(l+4)(l+5)} I_{l+3}^2 \\ &\quad - \frac{1}{2} (l+2)(l+3) \sqrt{l(l+1)} I_{l+3}^0 \end{aligned} \quad (\text{D.42})$$

$$\begin{aligned} \frac{\partial^3}{\partial x_2 \partial x_3^2} (I_l^1) &= -\frac{i}{2} \sqrt{l(l+1)(l+2)(l+3)(l+4)(l+5)} I_{l+3}^2 \\ &\quad - \frac{i}{2} (l+2)(l+3) \sqrt{l(l+1)} I_{l+3}^0 \end{aligned} \quad (\text{D.43})$$

$$\begin{aligned} \frac{\partial^3}{\partial x_1 \partial x_2 \partial x_3} (I_l^1) &= \frac{i}{4} \sqrt{l(l+2)(l+3)(l+4)(l+5)(l+6)} I_{l+3}^3 \\ &\quad + \frac{i}{4} (l+2) \sqrt{l(l+1)(l+3)(l+4)} I_{l+3}^{-1} \end{aligned} \quad (\text{D.44})$$

- $m = 2$

$$\begin{aligned} \frac{\partial^3}{\partial x_1^3} (I_l^2) &= \frac{1}{8} \sqrt{(l+3)(l+4)(l+5)(l+6)(l+7)(l+8)} I_{l+3}^5 \\ &\quad - \frac{3}{8} \sqrt{(l-1)l(l+3)(l+4)(l+5)(l+6)} I_{l+3}^3 \\ &\quad + \frac{3}{8} \sqrt{(l-1)l(l+1)(l+2)(l+3)(l+4)} I_{l+3}^1 \\ &\quad + \frac{1}{8} \sqrt{(l-1)l(l+1)(l+2)(l+3)(l+4)} I_{l+3}^{-1} \end{aligned} \quad (\text{D.45})$$

$$\begin{aligned} \frac{\partial^3}{\partial x_2^3} (I_l^2) &= \frac{i}{8} \sqrt{(l+3)(l+4)(l+5)(l+6)(l+7)(l+8)} I_{l+3}^5 \\ &\quad + \frac{3i}{8} \sqrt{(l-1)l(l+3)(l+4)(l+5)(l+6)} I_{l+3}^3 \\ &\quad + \frac{3i}{8} \sqrt{(l-1)l(l+1)(l+2)(l+3)(l+4)} I_{l+3}^1 \\ &\quad - \frac{i}{8} \sqrt{(l-1)l(l+1)(l+2)(l+3)(l+4)} I_{l+3}^{-1} \end{aligned} \quad (\text{D.46})$$

$$\frac{\partial^3}{\partial x_3^3} (I_l^2) = -\sqrt{(l-1)l(l+1)(l+3)(l+4)(l+5)} I_{l+3}^2 \quad (\text{D.47})$$

$$\begin{aligned} \frac{\partial^3}{\partial x_1^2 \partial x_2} (I_l^2) &= -\frac{i}{8} \sqrt{(l+3)(l+4)(l+5)(l+6)(l+7)(l+8)} I_{l+3}^5 \\ &\quad + \frac{i}{8} \sqrt{(l-1)l(l+3)(l+4)(l+5)(l+6)} I_{l+3}^3 \\ &\quad + \frac{i}{8} \sqrt{(l-1)l(l+1)(l+2)(l+3)(l+4)} I_{l+3}^1 \\ &\quad + \frac{i}{8} \sqrt{(l-1)l(l+1)(l+2)(l+3)(l+4)} I_{l+3}^{-1} \end{aligned} \quad (\text{D.48})$$

$$\begin{aligned}
\frac{\partial^3}{\partial x_1^2 \partial x_3} (I_l^2) &= -\frac{1}{4} \sqrt{(l-1)(l+3)(l+4)(l+5)(l+6)(l+7)} I_{l+3}^4 \\
&\quad + \frac{1}{2} \sqrt{(l-1)l(l+1)(l+3)(l+4)(l+5)} I_{l+3}^2 \\
&\quad - \frac{1}{4} (l+3) \sqrt{(l-1)l(l+1)(l+2)} I_{l+3}^0 \quad (\text{D.49})
\end{aligned}$$

$$\begin{aligned}
\frac{\partial^3}{\partial x_1 \partial x_2^2} (I_l^2) &= -\frac{1}{8} \sqrt{(l+3)(l+4)(l+5)(l+6)(l+7)(l+8)} I_{l+3}^5 \\
&\quad - \frac{1}{8} \sqrt{(l-1)l(l+3)(l+4)(l+5)(l+6)} I_{l+3}^3 \\
&\quad + \frac{1}{8} \sqrt{(l-1)l(l+1)(l+2)(l+3)(l+4)} I_{l+3}^1 \\
&\quad - \frac{1}{8} \sqrt{(l-1)l(l+1)(l+2)(l+3)(l+4)} I_{l+3}^{-1} \quad (\text{D.50})
\end{aligned}$$

$$\begin{aligned}
\frac{\partial^3}{\partial x_2^2 \partial x_3} (I_l^2) &= \frac{1}{4} \sqrt{(l-1)(l+3)(l+4)(l+5)(l+6)(l+7)} I_{l+3}^4 \\
&\quad + \frac{1}{2} \sqrt{(l-1)l(l+1)(l+3)(l+4)(l+5)} I_{l+3}^2 \\
&\quad + \frac{1}{4} (l+3) \sqrt{(l-1)l(l+1)(l+2)} I_{l+3}^0 \quad (\text{D.51})
\end{aligned}$$

$$\begin{aligned}
\frac{\partial^3}{\partial x_1 \partial x_3^2} (I_l^2) &= \frac{1}{2} \sqrt{(l-1)l(l+3)(l+4)(l+5)(l+6)} I_{l+3}^3 \\
&\quad - \frac{1}{2} \sqrt{(l-1)l(l+1)(l+2)(l+3)(l+4)} I_{l+3}^1 \quad (\text{D.52})
\end{aligned}$$

$$\begin{aligned}
\frac{\partial^3}{\partial x_2 \partial x_3^2} (I_l^2) &= -\frac{i}{2} \sqrt{(l-1)l(l+3)(l+4)(l+5)(l+6)} I_{l+3}^3 \\
&\quad - \frac{i}{2} \sqrt{(l-1)l(l+1)(l+2)(l+3)(l+4)} I_{l+3}^1 \quad (\text{D.53})
\end{aligned}$$

$$\begin{aligned}
\frac{\partial^3}{\partial x_1 \partial x_2 \partial x_3} (I_l^2) &= \frac{i}{4} \sqrt{(l-1)(l+3)(l+4)(l+5)(l+6)(l+7)} I_{l+3}^4 \\
&\quad - \frac{i}{4} (l+3) \sqrt{(l-1)l(l+1)(l+2)} I_{l+3}^0 \quad (\text{D.54})
\end{aligned}$$

- $m \geq 3$

$$\begin{aligned}
\frac{\partial^3}{\partial x_1^3}(I_l^m) &= \frac{1}{8}\sqrt{(l+m+1)(l+m+2)(l+m+3)(l+m+4)(l+m+5)(l+m+6)}I_{l+3}^{m+3} \\
&- \frac{3}{8}\sqrt{(l-m+1)(l-m+2)(l+m+1)(l+m+2)(l+m+3)(l+m+4)}I_{l+3}^{m+1} \\
&+ \frac{3}{8}\sqrt{(l-m+1)(l-m+2)(l-m+3)(l-m+4)(l+m+1)(l+m+2)}I_{l+3}^{m-1} \\
&- \frac{1}{8}\sqrt{(l-m+1)(l-m+2)(l-m+3)(l-m+4)(l-m+5)(l-m+6)}I_{l+3}^{m-3}
\end{aligned} \tag{D.55}$$

$$\begin{aligned}
\frac{\partial^3}{\partial x_2^3}(I_l^m) &= \frac{i}{8}\sqrt{(l+m+1)(l+m+2)(l+m+3)(l+m+4)(l+m+5)(l+m+6)}I_{l+3}^{m+3} \\
&+ \frac{3i}{8}\sqrt{(l-m+1)(l-m+2)(l+m+1)(l+m+2)(l+m+3)(l+m+4)}I_{l+3}^{m+1} \\
&+ \frac{3i}{8}\sqrt{(l-m+1)(l-m+2)(l-m+3)(l-m+4)(l+m+1)(l+m+2)}I_{l+3}^{m-1} \\
&+ \frac{i}{8}\sqrt{(l-m+1)(l-m+2)(l-m+3)(l-m+4)(l-m+5)(l-m+6)}I_{l+3}^{m-3}
\end{aligned} \tag{D.56}$$

$$\frac{\partial^3}{\partial x_3^3}(I_l^m) = -\sqrt{(l-m+1)(l-m+2)(l-m+3)(l+m+1)(l+m+2)(l+m+3)}I_{l+3}^m \tag{D.57}$$

$$\begin{aligned}
\frac{\partial^3}{\partial x_1^2 \partial x_2}(I_l^m) &= -\frac{i}{8}\sqrt{(l+m+1)(l+m+2)(l+m+3)(l+m+4)(l+m+5)(l+m+6)}I_{l+3}^{m+3} \\
&+ \frac{i}{8}\sqrt{(l-m+1)(l-m+2)(l+m+1)(l+m+2)(l+m+3)(l+m+4)}I_{l+3}^{m+1} \\
&+ \frac{i}{8}\sqrt{(l-m+1)(l-m+2)(l-m+3)(l-m+4)(l+m+1)(l+m+2)}I_{l+3}^{m-1} \\
&- \frac{i}{8}\sqrt{(l-m+1)(l-m+2)(l-m+3)(l-m+4)(l-m+5)(l-m+6)}I_{l+3}^{m-3}
\end{aligned} \tag{D.58}$$

$$\begin{aligned}
\frac{\partial^3}{\partial x_1^2 \partial x_3}(I_l^m) &= -\frac{1}{4}\sqrt{(l-m+1)(l+m+1)(l+m+2)(l+m+3)(l+m+4)(l+m+5)}I_{l+3}^{m+2} \\
&+ \frac{1}{2}\sqrt{(l-m+1)(l-m+2)(l-m+3)(l+m+1)(l+m+2)(l+m+3)}I_{l+3}^m \\
&- \frac{1}{4}\sqrt{(l-m+1)(l-m+2)(l-m+3)(l-m+4)(l-m+5)(l+m+1)}I_{l+3}^{m-2}
\end{aligned} \tag{D.59}$$

$$\begin{aligned}
\frac{\partial^3}{\partial x_1 \partial x_2^2} (I_l^m) &= -\frac{1}{8} \sqrt{(l+m+1)(l+m+2)(l+m+3)(l+m+4)(l+m+5)(l+m+6)} I_{l+3}^{m+3} \\
&- \frac{1}{8} \sqrt{(l-m+1)(l-m+2)(l+m+1)(l+m+2)(l+m+3)(l+m+4)} I_{l+3}^{m+1} \\
&+ \frac{1}{8} \sqrt{(l-m+1)(l-m+2)(l-m+3)(l-m+4)(l+m+1)(l+m+2)} I_{l+3}^{m-1} \\
&+ \frac{1}{8} \sqrt{(l-m+1)(l-m+2)(l-m+3)(l-m+4)(l-m+5)(l-m+6)} I_{l+3}^{m-3}
\end{aligned} \tag{D.60}$$

$$\begin{aligned}
\frac{\partial^3}{\partial x_2^2 \partial x_3} (I_l^m) &= \frac{1}{4} \sqrt{(l-m+1)(l+m+1)(l+m+2)(l+m+3)(l+m+4)(l+m+5)} I_{l+3}^{m+2} \\
&+ \frac{1}{2} \sqrt{(l-m+1)(l-m+2)(l-m+3)(l+m+1)(l+m+2)(l+m+3)} I_{l+3}^m \\
&+ \frac{1}{4} \sqrt{(l-m+1)(l-m+2)(l-m+3)(l-m+4)(l-m+5)(l+m+1)} I_{l+3}^{m-2}
\end{aligned} \tag{D.61}$$

$$\begin{aligned}
\frac{\partial^3}{\partial x_1 \partial x_3^2} (I_l^m) &= \frac{1}{2} \sqrt{(l-m+1)(l-m+2)(l+m+1)(l+m+2)(l+m+3)(l+m+4)} I_{l+3}^{m+1} \\
&- \frac{1}{2} \sqrt{(l-m+1)(l-m+2)(l-m+3)(l-m+4)(l+m+1)(l+m+2)} I_{l+3}^{m-1}
\end{aligned} \tag{D.62}$$

$$\begin{aligned}
\frac{\partial^3}{\partial x_2 \partial x_3^2} (I_l^m) &= -\frac{i}{2} \sqrt{(l-m+1)(l-m+2)(l+m+1)(l+m+2)(l+m+3)(l+m+4)} I_{l+3}^{m+1} \\
&- \frac{i}{2} \sqrt{(l-m+1)(l-m+2)(l-m+3)(l-m+4)(l+m+1)(l+m+2)} I_{l+3}^{m-1}
\end{aligned} \tag{D.63}$$

$$\begin{aligned}
\frac{\partial^3}{\partial x_1 \partial x_2 \partial x_3} (I_l^m) &= \frac{i}{4} \sqrt{(l-m+1)(l+m+1)(l+m+2)(l+m+3)(l+m+4)(l+m+5)} I_{l+3}^{m+2} \\
&- \frac{i}{4} \sqrt{(l-m+1)(l-m+2)(l-m+3)(l-m+4)(l-m+5)(l+m+1)} I_{l+3}^{m-2}
\end{aligned} \tag{D.64}$$

676 Appendix E. Derivatives of regular solid harmonics

677 Derivatives of regular solid harmonics are useful for the multipole expansion of the strain
678 field of a cavity (Eq. (23)) and a dislocation segment (Eqs. (28)-(29)). They can be
679 obtained by writing $R_l^m(x, \theta, \varphi) = x^{2l+1} I_l^m(x, \theta, \varphi)$, then using Eq. (B.6) and recursion
680 formulas (B.12) and (B.13). First and second derivatives are given in Ref. [27]. They
681 are recalled here for the sake of completeness.

682 *First derivatives*

- $m = 0$

$$\frac{\partial}{\partial x_1}(R_l^0) = \frac{1}{2}\sqrt{l(l-1)}(R_{l-1}^{-1} + R_{l-1}^1) \quad (\text{E.1})$$

$$\frac{\partial}{\partial x_2}(R_l^0) = -\frac{i}{2}\sqrt{l(l-1)}(R_{l-1}^1 - R_{l-1}^{-1}) \quad (\text{E.2})$$

$$\frac{\partial}{\partial x_3}(R_l^0) = lR_{l-1}^0 \quad (\text{E.3})$$

- $m \geq 1$

$$\frac{\partial}{\partial x_1}(R_l^m) = \frac{1}{2}\left(\sqrt{(l-m)(l-m-1)}R_{l-1}^{m+1} - \sqrt{(l+m)(l+m-1)}R_{l-1}^{m-1}\right) \quad (\text{E.4})$$

$$\frac{\partial}{\partial x_2}(R_l^m) = -\frac{i}{2}\left(\sqrt{(l-m)(l-m-1)}R_{l-1}^{m+1} + \sqrt{(l+m)(l+m-1)}R_{l-1}^{m-1}\right) \quad (\text{E.5})$$

$$\frac{\partial}{\partial x_3}(R_l^m) = \sqrt{(l+m)(l-m)}R_{l-1}^m \quad (\text{E.6})$$

683 *Second derivatives*

- $m = 0$

$$\frac{\partial^2}{\partial x_1^2}(R_l^0) = \frac{1}{4}\sqrt{l(l-1)(l-2)(l-3)}(R_{l-2}^2 + R_{l-2}^{-2}) - \frac{1}{2}l(l-1)R_{l-2}^0 \quad (\text{E.7})$$

$$\frac{\partial^2}{\partial x_2^2}(R_l^0) = -\frac{1}{4}\sqrt{l(l-1)(l-2)(l-3)}(R_{l-2}^2 + R_{l-2}^{-2}) - \frac{1}{2}l(l-1)R_{l-2}^0 \quad (\text{E.8})$$

$$\frac{\partial^2}{\partial x_3^2}(R_l^0) = l(l-1)R_{l-2}^0 \quad (\text{E.9})$$

$$\frac{\partial^2}{\partial x_1 \partial x_2}(R_l^0) = -\frac{i}{4}\sqrt{l(l-1)(l-2)(l-3)}(R_{l-2}^2 - R_{l-2}^{-2}) \quad (\text{E.10})$$

$$\frac{\partial^2}{\partial x_2 \partial x_3}(R_l^0) = -\frac{i}{2}l\sqrt{(l-1)(l-2)}(R_{l-2}^1 - R_{l-2}^{-1}) \quad (\text{E.11})$$

$$\frac{\partial^2}{\partial x_1 \partial x_3}(R_l^0) = \frac{1}{2}l\sqrt{(l-1)(l-2)}(R_{l-2}^1 + R_{l-2}^{-1}) \quad (\text{E.12})$$

- $m = 1$

$$\begin{aligned} \frac{\partial^2}{\partial x_1^2}(R_l^1) = & \frac{1}{4}\sqrt{(l-1)(l-2)(l-3)(l-4)}R_{l-2}^3 - \frac{1}{2}\sqrt{(l+1)l(l-1)(l-2)}R_{l-2}^1 \\ & - \frac{1}{4}\sqrt{(l+1)l(l-1)(l-2)}R_{l-2}^{-1} \quad (\text{E.13}) \end{aligned}$$

$$\begin{aligned} \frac{\partial^2}{\partial x_2^2}(R_l^1) = & -\frac{1}{4}\sqrt{(l-1)(l-2)(l-3)(l-4)}R_{l-2}^3 - \frac{1}{2}\sqrt{(l+1)l(l-1)(l-2)}R_{l-2}^1 \\ & + \frac{1}{4}\sqrt{(l+1)l(l-1)(l-2)}R_{l-2}^{-1} \quad (\text{E.14}) \end{aligned}$$

$$\frac{\partial^2}{\partial x_3^2}(R_l^1) = \sqrt{(l+1)l(l-1)(l-2)}R_{l-2}^1 \quad (\text{E.15})$$

$$\frac{\partial^2}{\partial x_1 \partial x_2}(R_l^1) = -\frac{i}{4}\sqrt{(l-1)(l-2)(l-3)(l-4)}R_{l-2}^3 - \frac{i}{4}\sqrt{(l+1)l(l-1)(l-2)}R_{l-2}^{-1} \quad (\text{E.16})$$

$$\frac{\partial^2}{\partial x_2 \partial x_3}(R_l^1) = -\frac{i}{2}\sqrt{(l+1)(l-1)(l-2)(l-3)}R_{l-2}^2 - \frac{i}{2}\sqrt{(l+1)l(l-1)^2}R_{l-2}^0 \quad (\text{E.17})$$

$$\frac{\partial^2}{\partial x_1 \partial x_3}(R_l^1) = \frac{1}{2}\sqrt{(l+1)(l-1)(l-2)(l-3)}R_{l-2}^2 - \frac{1}{2}\sqrt{(l+1)l(l-1)^2}R_{l-2}^0 \quad (\text{E.18})$$

• $m \geq 2$

$$\begin{aligned} \frac{\partial^2}{\partial x_1^2}(R_l^m) &= \frac{1}{4}\sqrt{(l-m)(l-m-1)(l-m-2)(l-m-3)}R_{l-2}^{m+2} \\ &\quad - \frac{1}{2}\sqrt{(l+m)(l+m-1)(l-m)(l-m-1)}R_{l-2}^m \\ &\quad + \frac{1}{4}\sqrt{(l+m)(l+m-1)(l+m-2)(l+m-3)}R_{l-2}^{m-2} \end{aligned} \quad (\text{E.19})$$

$$\begin{aligned} \frac{\partial^2}{\partial x_2^2}(R_l^m) &= -\frac{1}{4}\sqrt{(l-m)(l-m-1)(l-m-2)(l-m-3)}R_{l-2}^{m+2} \\ &\quad - \frac{1}{2}\sqrt{(l+m)(l+m-1)(l-m)(l-m-1)}R_{l-2}^m \\ &\quad - \frac{1}{4}\sqrt{(l+m)(l+m-1)(l+m-2)(l+m-3)}R_{l-2}^{m-2} \end{aligned} \quad (\text{E.20})$$

$$\frac{\partial^2}{\partial x_3^2}(R_l^m) = \sqrt{(l+m)(l+m-1)(l-m)(l-m-1)}R_{l-2}^m \quad (\text{E.21})$$

$$\begin{aligned} \frac{\partial^2}{\partial x_1 \partial x_2}(R_l^m) &= -\frac{i}{4}\sqrt{(l-m)(l-m-1)(l-m-2)(l-m-3)}R_{l-2}^{m+2} \\ &\quad + \frac{i}{4}\sqrt{(l+m)(l+m-1)(l+m-2)(l+m-3)}R_{l-2}^{m-2} \end{aligned} \quad (\text{E.22})$$

$$\begin{aligned} \frac{\partial^2}{\partial x_2 \partial x_3}(R_l^m) &= -\frac{i}{2}\sqrt{(l+m)(l-m)(l-m-1)(l-m-2)}R_{l-2}^{m+1} \\ &\quad - \frac{i}{2}\sqrt{(l+m)(l+m-1)(l+m-2)(l-m)}R_{l-2}^{m-1} \end{aligned} \quad (\text{E.23})$$

$$\begin{aligned} \frac{\partial^2}{\partial x_1 \partial x_3}(R_l^m) &= \frac{1}{2}\sqrt{(l+m)(l-m)(l-m-1)(l-m-2)}R_{l-2}^{m+1} \\ &\quad - \frac{1}{2}\sqrt{(l+m)(l+m-1)(l+m-2)(l-m)}R_{l-2}^{m-1} \end{aligned} \quad (\text{E.24})$$

684 *Third derivatives*

- $m = 0$

$$\begin{aligned} \frac{\partial^3}{\partial x_1^3}(R_l^0) &= \frac{1}{8}\sqrt{l(l-1)(l-2)(l-3)(l-4)(l-5)}(R_{l-3}^3 + R_{l-3}^{-3}) \\ &\quad - \frac{3}{8}l(l-1)\sqrt{(l-2)(l-3)}(R_{l-3}^1 + R_{l-3}^{-1}) \quad (\text{E.25}) \end{aligned}$$

$$\begin{aligned} \frac{\partial^3}{\partial x_2^3}(R_l^0) &= \frac{i}{8}\sqrt{l(l-1)(l-2)(l-3)(l-4)(l-5)}(R_{l-3}^3 - R_{l-3}^{-3}) \\ &\quad + \frac{3i}{8}l(l-1)\sqrt{(l-2)(l-3)}(R_{l-3}^1 - R_{l-3}^{-1}) \quad (\text{E.26}) \end{aligned}$$

$$\frac{\partial^3}{\partial x_3^3}(R_l^0) = l(l-1)(l-2)R_{l-3}^0 \quad (\text{E.27})$$

$$\begin{aligned} \frac{\partial^3}{\partial x_1^2 \partial x_2}(R_l^0) &= -\frac{i}{8}\sqrt{l(l-1)(l-2)(l-3)(l-4)(l-5)}(R_{l-3}^3 - R_{l-3}^{-3}) \\ &\quad + \frac{i}{8}l(l-1)\sqrt{(l-2)(l-3)}(R_{l-3}^1 - R_{l-3}^{-1}) \quad (\text{E.28}) \end{aligned}$$

$$\begin{aligned} \frac{\partial^3}{\partial x_1^2 \partial x_3}(R_l^0) &= \frac{1}{4}\sqrt{l^2(l-1)(l-2)(l-3)(l-4)}(R_{l-3}^2 + R_{l-3}^{-2}) - \frac{1}{2}l(l-1)(l-2)R_{l-3}^0 \\ &\quad (\text{E.29}) \end{aligned}$$

$$\begin{aligned} \frac{\partial^3}{\partial x_1 \partial x_2^2}(R_l^0) &= -\frac{1}{8}\sqrt{l(l-1)(l-2)(l-3)(l-4)(l-5)}(R_{l-3}^3 + R_{l-3}^{-3}) \\ &\quad - \frac{1}{8}l(l-1)\sqrt{(l-2)(l-3)}(R_{l-3}^1 + R_{l-3}^{-1}) \quad (\text{E.30}) \end{aligned}$$

$$\begin{aligned} \frac{\partial^3}{\partial x_2^2 \partial x_3}(R_l^0) &= -\frac{1}{4}\sqrt{l^2(l-1)(l-2)(l-3)(l-4)}(R_{l-3}^2 + R_{l-3}^{-2}) - \frac{1}{2}l(l-1)(l-2)R_{l-3}^0 \\ &\quad (\text{E.31}) \end{aligned}$$

$$\frac{\partial^3}{\partial x_1 \partial x_3^2}(R_l^0) = \frac{1}{2}l(l-1)\sqrt{(l-2)(l-3)}(R_{l-3}^1 + R_{l-3}^{-1}) \quad (\text{E.32})$$

$$\frac{\partial^3}{\partial x_2 \partial x_3^2}(R_l^0) = -\frac{i}{2}l(l-1)\sqrt{(l-2)(l-3)}(R_{l-3}^1 - R_{l-3}^{-1}) \quad (\text{E.33})$$

$$\frac{\partial^3}{\partial x_1 \partial x_2 \partial x_3}(R_l^0) = -\frac{i}{4}\sqrt{l^2(l-1)(l-2)(l-3)(l-4)}(R_{l-3}^2 - R_{l-3}^{-2}) \quad (\text{E.34})$$

- $m = 1$

$$\begin{aligned} \frac{\partial^3}{\partial x_1^3}(R_l^1) &= \frac{1}{8}\sqrt{(l-1)(l-2)(l-3)(l-4)(l-5)(l-6)}R_{l-3}^4 \\ &\quad - \frac{3}{8}\sqrt{(l+1)l(l-1)(l-2)(l-3)(l-4)}R_{l-3}^2 \\ &\quad + \frac{3}{8}\sqrt{(l+1)l(l-1)(l-2)}R_{l-3}^0 \\ &\quad - \frac{1}{8}\sqrt{(l+1)l(l-1)(l-2)(l-3)(l-4)}R_{l-3}^{-2} \quad (\text{E.35}) \end{aligned}$$

$$\begin{aligned}
\frac{\partial^3}{\partial x_2^3}(R_l^1) &= \frac{i}{8}\sqrt{(l-1)(l-2)(l-3)(l-4)(l-5)(l-6)}R_{l-3}^4 \\
&\quad + \frac{3i}{8}\sqrt{(l+1)l(l-1)(l-2)(l-3)(l-4)}R_{l-3}^2 \\
&\quad + \frac{3i}{8}\sqrt{(l+1)l(l-1)(l-2)}R_{l-3}^0 \\
&\quad + \frac{i}{8}\sqrt{(l+1)l(l-1)(l-2)(l-3)(l-4)}R_{l-3}^{-2} \quad (\text{E.36})
\end{aligned}$$

$$\frac{\partial^3}{\partial x_3^3}(R_l^1) = \sqrt{(l+1)l(l-1)^2(l-2)(l-3)}R_{l-3}^1 \quad (\text{E.37})$$

$$\begin{aligned}
\frac{\partial^3}{\partial x_1^2 \partial x_2}(R_l^1) &= -\frac{i}{8}\sqrt{(l-1)(l-2)(l-3)(l-4)(l-5)(l-6)}R_{l-3}^4 \\
&\quad + \frac{i}{8}\sqrt{(l+1)l(l-1)(l-2)(l-3)(l-4)}R_{l-3}^2 \\
&\quad + \frac{i}{8}\sqrt{(l+1)l(l-1)(l-2)}R_{l-3}^0 \\
&\quad - \frac{i}{8}\sqrt{(l+1)l(l-1)(l-2)(l-3)(l-4)}R_{l-3}^{-2} \quad (\text{E.38})
\end{aligned}$$

$$\begin{aligned}
\frac{\partial^3}{\partial x_1^2 \partial x_3}(R_l^1) &= \frac{1}{4}\sqrt{(l+1)l(l-1)(l-2)(l-3)(l-4)(l-5)}R_{l-3}^3 \\
&\quad - \frac{1}{2}\sqrt{(l+1)l(l-1)^2(l-2)(l-3)}R_{l-3}^1 \\
&\quad - \frac{1}{4}\sqrt{(l+1)l(l-1)^2(l-2)(l-3)}R_{l-3}^{-1} \quad (\text{E.39})
\end{aligned}$$

$$\begin{aligned}
\frac{\partial^3}{\partial x_1 \partial x_2^2}(R_l^1) &= -\frac{1}{8}\sqrt{(l-1)(l-2)(l-3)(l-4)(l-5)(l-6)}R_{l-3}^4 \\
&\quad - \frac{1}{8}\sqrt{(l+1)l(l-1)(l-2)(l-3)(l-4)}R_{l-3}^2 \\
&\quad + \frac{1}{8}\sqrt{(l+1)l(l-1)(l-2)}R_{l-3}^0 \\
&\quad + \frac{1}{8}\sqrt{(l+1)l(l-1)(l-2)(l-3)(l-4)}R_{l-3}^{-2} \quad (\text{E.40})
\end{aligned}$$

$$\begin{aligned}
\frac{\partial^3}{\partial x_2^2 \partial x_3}(R_l^1) &= -\frac{1}{4}\sqrt{(l+1)l(l-1)(l-2)(l-3)(l-4)(l-5)}R_{l-3}^3 \\
&\quad - \frac{1}{2}\sqrt{(l+1)l(l-1)^2(l-2)(l-3)}R_{l-3}^1 \\
&\quad + \frac{1}{4}\sqrt{(l+1)l(l-1)^2(l-2)(l-3)}R_{l-3}^{-1} \quad (\text{E.41})
\end{aligned}$$

$$\frac{\partial^3}{\partial x_1 \partial x_3^2}(R_l^1) = \frac{1}{2} \sqrt{(l+1)l(l-1)(l-2)(l-3)(l-4)} R_{l-3}^2 - \frac{1}{2} \sqrt{(l+1)l(l-1)(l-2)} R_{l-3}^0 \quad (\text{E.42})$$

$$\frac{\partial^3}{\partial x_2 \partial x_3^2}(R_l^1) = -\frac{i}{2} \sqrt{(l+1)l(l-1)(l-2)(l-3)(l-4)} R_{l-3}^2 - \frac{i}{2} \sqrt{(l+1)l(l-1)(l-2)} R_{l-3}^0 \quad (\text{E.43})$$

$$\begin{aligned} \frac{\partial^3}{\partial x_1 \partial x_2 \partial x_3}(R_l^1) &= -\frac{i}{4} \sqrt{(l+1)(l-1)(l-2)(l-3)(l-4)(l-5)} R_{l-3}^3 \\ &\quad - \frac{i}{4} \sqrt{(l+1)l(l-1)^2(l-2)(l-3)} R_{l-3}^{-1} \end{aligned} \quad (\text{E.44})$$

• $m = 2$

$$\begin{aligned} \frac{\partial^3}{\partial x_1^3}(R_l^2) &= \frac{1}{8} \sqrt{(l-2)(l-3)(l-4)(l-5)(l-6)(l-7)} R_{l-3}^5 \\ &\quad - \frac{3}{8} \sqrt{(l+2)(l+1)(l-2)(l-3)(l-4)(l-5)} R_{l-3}^3 \\ &\quad + \frac{3}{8} \sqrt{(l+2)(l+1)l(l-1)(l-2)(l-3)} R_{l-3}^1 \\ &\quad + \frac{1}{8} \sqrt{(l+2)(l+1)l(l-1)(l-2)(l-3)} R_{l-3}^{-1} \end{aligned} \quad (\text{E.45})$$

$$\begin{aligned} \frac{\partial^3}{\partial x_2^3}(R_l^2) &= \frac{i}{8} \sqrt{(l-2)(l-3)(l-4)(l-5)(l-6)(l-7)} R_{l-3}^5 \\ &\quad + \frac{3i}{8} \sqrt{(l+2)(l+1)(l-2)(l-3)(l-4)(l-5)} R_{l-3}^3 \\ &\quad + \frac{3i}{8} \sqrt{(l+2)(l+1)l(l-1)(l-2)(l-3)} R_{l-3}^1 \\ &\quad - \frac{i}{8} \sqrt{(l+2)(l+1)l(l-1)(l-2)(l-3)} R_{l-3}^{-1} \end{aligned} \quad (\text{E.46})$$

$$\frac{\partial^3}{\partial x_3^3}(R_l^2) = \sqrt{(l+2)(l+1)l(l-2)(l-3)(l-4)} R_{l-3}^2 \quad (\text{E.47})$$

$$\begin{aligned} \frac{\partial^3}{\partial x_1^2 \partial x_2}(R_l^2) &= -\frac{i}{8} \sqrt{(l-2)(l-3)(l-4)(l-5)(l-6)(l-7)} R_{l-3}^5 \\ &\quad + \frac{i}{8} \sqrt{(l+2)(l+1)(l-2)(l-3)(l-4)(l-5)} R_{l-3}^3 \\ &\quad + \frac{i}{8} \sqrt{(l+2)(l+1)l(l-1)(l-2)(l-3)} R_{l-3}^1 \\ &\quad + \frac{i}{8} \sqrt{(l+2)(l+1)l(l-1)(l-2)(l-3)} R_{l-3}^{-1} \end{aligned} \quad (\text{E.48})$$

$$\begin{aligned} \frac{\partial^3}{\partial x_1^2 \partial x_3}(R_l^2) &= \frac{1}{4} \sqrt{(l+2)(l-2)(l-3)(l-4)(l-5)(l-6)} R_{l-3}^4 \\ &\quad - \frac{1}{2} \sqrt{(l+2)(l+1)l(l-2)(l-3)(l-4)} R_{l-3}^2 \\ &\quad + \frac{1}{4} \sqrt{(l+2)(l+1)l(l-1)(l-2)^2} R_{l-3}^0 \end{aligned} \quad (\text{E.49})$$

$$\begin{aligned}
\frac{\partial^3}{\partial x_1 \partial x_2^2}(R_l^2) &= -\frac{1}{8}\sqrt{(l-2)(l-3)(l-4)(l-5)(l-6)(l-7)}R_{l-3}^5 \\
&\quad -\frac{1}{8}\sqrt{(l+2)(l+1)(l-2)(l-3)(l-4)(l-5)}R_{l-3}^3 \\
&\quad +\frac{1}{8}\sqrt{(l+2)(l+1)l(l-1)(l-2)(l-3)}R_{l-3}^1 \\
&\quad -\frac{1}{8}\sqrt{(l+2)(l+1)l(l-1)(l-2)(l-3)}R_{l-3}^{-1} \quad (\text{E.50})
\end{aligned}$$

$$\begin{aligned}
\frac{\partial^3}{\partial x_2^2 \partial x_3}(R_l^2) &= -\frac{1}{4}\sqrt{(l+2)(l-2)(l-3)(l-4)(l-5)(l-6)}R_{l-3}^4 \\
&\quad -\frac{1}{2}\sqrt{(l+2)(l+1)l(l-2)(l-3)(l-4)}R_{l-3}^2 \\
&\quad -\frac{1}{4}\sqrt{(l+2)(l+1)l(l-1)(l-2)^2}R_{l-3}^0 \quad (\text{E.51})
\end{aligned}$$

$$\begin{aligned}
\frac{\partial^3}{\partial x_1 \partial x_3^2}(R_l^2) &= \frac{1}{2}\sqrt{(l+2)(l+1)(l-2)(l-3)(l-4)(l-5)}R_{l-3}^3 \\
&\quad -\frac{1}{2}\sqrt{(l+2)(l+1)l(l-1)(l-2)(l-3)}R_{l-3}^1 \quad (\text{E.52})
\end{aligned}$$

$$\begin{aligned}
\frac{\partial^3}{\partial x_2 \partial x_3^2}(R_l^2) &= -\frac{i}{2}\sqrt{(l+2)(l+1)(l-2)(l-3)(l-4)(l-5)}R_{l-3}^3 \\
&\quad -\frac{i}{2}\sqrt{(l+2)(l+1)l(l-1)(l-2)(l-3)}R_{l-3}^1 \quad (\text{E.53})
\end{aligned}$$

$$\begin{aligned}
\frac{\partial^3}{\partial x_1 \partial x_2 \partial x_3}(R_l^2) &= -\frac{i}{4}\sqrt{(l+2)(l-2)(l-3)(l-4)(l-5)(l-6)}R_{l-3}^4 \\
&\quad +\frac{i}{4}\sqrt{(l+2)(l+1)l(l-1)(l-2)^2}R_{l-3}^0 \quad (\text{E.54})
\end{aligned}$$

- $m \geq 3$

$$\begin{aligned}
\frac{\partial^3}{\partial x_1^3}(R_l^m) &= \frac{1}{8}\sqrt{(l-m)(l-m-1)(l-m-2)(l-m-3)(l-m-4)(l-m-5)}R_{l-3}^{m+3} \\
&\quad -\frac{3}{8}\sqrt{(l+m)(l+m-1)(l-m)(l-m-1)(l-m-2)(l-m-3)}R_{l-3}^{m+1} \\
&\quad +\frac{3}{8}\sqrt{(l+m)(l+m-1)(l+m-2)(l+m-3)(l-m)(l-m-1)}R_{l-3}^{m-1} \\
&\quad -\frac{1}{8}\sqrt{(l+m)(l+m-1)(l+m-2)(l+m-3)(l+m-4)(l+m-5)}R_{l-3}^{m-3} \\
&\hspace{15em} (\text{E.55})
\end{aligned}$$

$$\begin{aligned}
\frac{\partial^3}{\partial x_2^3}(R_l^m) &= \frac{i}{8}\sqrt{(l-m)(l-m-1)(l-m-2)(l-m-3)(l-m-4)(l-m-5)}R_{l-3}^{m+3} \\
&+ \frac{3i}{8}\sqrt{(l+m)(l+m-1)(l-m)(l-m-1)(l-m-2)(l-m-3)}R_{l-3}^{m+1} \\
&+ \frac{3i}{8}\sqrt{(l+m)(l+m-1)(l+m-2)(l+m-3)(l-m)(l-m-1)}R_{l-3}^{m-1} \\
&+ \frac{i}{8}\sqrt{(l+m)(l+m-1)(l+m-2)(l+m-3)(l+m-4)(l+m-5)}R_{l-3}^{m-3}
\end{aligned} \tag{E.56}$$

$$\frac{\partial^3}{\partial x_3^3}(R_l^m) = \sqrt{(l+m)(l+m-1)(l+m-2)(l-m)(l-m-1)(l-m-2)}R_{l-3}^m \tag{E.57}$$

$$\begin{aligned}
\frac{\partial^3}{\partial x_1^2 \partial x_2}(R_l^m) &= -\frac{i}{8}\sqrt{(l-m)(l-m-1)(l-m-2)(l-m-3)(l-m-4)(l-m-5)}R_{l-3}^{m+3} \\
&+ \frac{i}{8}\sqrt{(l+m)(l+m-1)(l-m)(l-m-1)(l-m-2)(l-m-3)}R_{l-3}^{m+1} \\
&+ \frac{i}{8}\sqrt{(l+m)(l+m-1)(l+m-2)(l+m-3)(l-m)(l-m-1)}R_{l-3}^{m-1} \\
&- \frac{i}{8}\sqrt{(l+m)(l+m-1)(l+m-2)(l+m-3)(l+m-4)(l+m-5)}R_{l-3}^{m-3}
\end{aligned} \tag{E.58}$$

$$\begin{aligned}
\frac{\partial^3}{\partial x_1^2 \partial x_3}(R_l^m) &= \frac{1}{4}\sqrt{(l+m)(l-m)(l-m-1)(l-m-2)(l-m-3)(l-m-4)}R_{l-3}^{m+2} \\
&- \frac{1}{2}\sqrt{(l+m)(l+m-1)(l+m-2)(l-m)(l-m-1)(l-m-2)}R_{l-3}^m \\
&+ \frac{1}{4}\sqrt{(l+m)(l+m-1)(l+m-2)(l+m-3)(l+m-4)(l-m)}R_{l-3}^{m-2}
\end{aligned} \tag{E.59}$$

$$\begin{aligned}
\frac{\partial^3}{\partial x_1 \partial x_2^2}(R_l^m) &= -\frac{1}{8}\sqrt{(l-m)(l-m-1)(l-m-2)(l-m-3)(l-m-4)(l-m-5)}R_{l-3}^{m+3} \\
&- \frac{1}{8}\sqrt{(l+m)(l+m-1)(l-m)(l-m-1)(l-m-2)(l-m-3)}R_{l-3}^{m+1} \\
&+ \frac{1}{8}\sqrt{(l+m)(l+m-1)(l+m-2)(l+m-3)(l-m)(l-m-1)}R_{l-3}^{m-1} \\
&+ \frac{1}{8}\sqrt{(l+m)(l+m-1)(l+m-2)(l+m-3)(l+m-4)(l+m-5)}R_{l-3}^{m-3}
\end{aligned} \tag{E.60}$$

$$\begin{aligned}
\frac{\partial^3}{\partial x_2^2 \partial x_3}(R_l^m) &= -\frac{1}{4}\sqrt{(l+m)(l-m)(l-m-1)(l-m-2)(l-m-3)(l-m-4)}R_{l-3}^{m+2} \\
&- \frac{1}{2}\sqrt{(l+m)(l+m-1)(l+m-2)(l-m)(l-m-1)(l-m-2)}R_{l-3}^m \\
&- \frac{1}{4}\sqrt{(l+m)(l+m-1)(l+m-2)(l+m-3)(l+m-4)(l-m)}R_{l-3}^{m-2}
\end{aligned} \tag{E.61}$$

$$\begin{aligned} \frac{\partial^3}{\partial x_1 \partial x_2^2} (R_l^m) &= \frac{1}{2} \sqrt{(l+m)(l+m-1)(l-m)(l-m-1)(l-m-2)(l-m-3)} R_{l-3}^{m+1} \\ &- \frac{1}{2} \sqrt{(l+m)(l+m-1)(l+m-2)(l+m-3)(l-m)(l-m-1)} R_{l-3}^{m-1} \quad (\text{E.62}) \end{aligned}$$

$$\begin{aligned} \frac{\partial^3}{\partial x_2 \partial x_3^2} (R_l^m) &= -\frac{i}{2} \sqrt{(l+m)(l+m-1)(l-m)(l-m-1)(l-m-2)(l-m-3)} R_{l-3}^{m+1} \\ &- \frac{i}{2} \sqrt{(l+m)(l+m-1)(l+m-2)(l+m-3)(l-m)(l-m-1)} R_{l-3}^{m-1} \quad (\text{E.63}) \end{aligned}$$

$$\begin{aligned} \frac{\partial^3}{\partial x_1 \partial x_2 \partial x_3} (R_l^m) &= -\frac{i}{4} \sqrt{(l+m)(l-m)(l-m-1)(l-m-2)(l-m-3)(l-m-4)} R_{l-3}^{m+2} \\ &+ \frac{i}{4} \sqrt{(l+m)(l+m-1)(l+m-2)(l+m-3)(l+m-4)(l-m)} R_{l-3}^{m-2} \quad (\text{E.64}) \end{aligned}$$

685 Appendix F. Correction ε^0 to the dipolar field

686 The field which must be subtracted from the discrete sum of the dipolar field over
687 neighbour boxes, in order to get a periodic solution, has an analytical form if the sum is
688 performed over a cuboid domain centered on the simulation box [48]. We recall here its
689 expression for the sake of completeness. Let the dimensions of the summation domain
690 be l_1 , l_2 and l_3 . We have for the two components ε_{11}^0 and ε_{12}^0 (other terms are obtained
691 by cyclic permutation of indices):

$$\begin{aligned} \varepsilon_{11}^0 &= \frac{p_{11}}{2\pi(1-\nu)\mu} [2(1-2\nu)A(l_1, l_2, l_3) + B(l_1, l_2, l_3)] \\ &\quad - \frac{p_{22}}{2\pi(1-\nu)\mu} E(l_2, l_1, l_3) - \frac{p_{33}}{2\pi(1-\nu)\mu} E(l_3, l_1, l_2) \quad (\text{F.1}) \end{aligned}$$

692

$$\varepsilon_{12}^0 = \frac{p_{12}}{2\pi(1-\nu)\mu} [2(1-\nu)(A(l_1, l_2, l_3) + A(l_2, l_1, l_3)) - (E(l_1, l_2, l_3) + E(l_2, l_1, l_3))]. \quad (\text{F.2})$$

693 Functions A , B and E are given by

$$A(x, y, z) = \arctan \left(\frac{yz}{x\sqrt{x^2 + y^2 + z^2}} \right) \quad (\text{F.3})$$

$$B(x, y, z) = \frac{xyz(2x^2 + y^2 + z^2)}{(x^2 + y^2)(x^2 + z^2)\sqrt{x^2 + y^2 + z^2}} \quad (\text{F.4})$$

$$E(x, y, z) = \frac{xyz}{(x^2 + y^2)\sqrt{x^2 + y^2 + z^2}}. \quad (\text{F.5})$$

References

- [1] S. J. Zinkle. Radiation-induced effects on microstructure. In R. J. M. Konings and R. E. Stoller, editors, *Comprehensive Nuclear Materials*, chapter 1.04, page 91. Elsevier, second edition, 2020.
- [2] A. D. Brailsford and R. Bullough. The rate theory of swelling due to void growth in irradiated metals. *J. Nucl. Mater.*, 44:121, 1972.
- [3] T. Jourdan and M. Nastar. On the relative contributions of point defect clusters to macroscopic swelling of metals. *J. Appl. Phys.*, 131:225103, 2022.
- [4] M. J. Caturla, N. Soneda, E. Alonso, B. D. Wirth, T. Diaz de la Rubia, and J. M. Perlado. Comparative study of radiation damage accumulation in Cu and Fe. *J. Nucl. Mater.*, 276:13, 2000.
- [5] C. Domain, C. S. Becquart, and L. Malerba. Simulation of radiation damage in Fe alloys: an object kinetic Monte Carlo approach. *J. Nucl. Mater.*, 335:121, 2004.
- [6] J. Dalla Torre, C.-C. Fu, F. Willaime, A. Barbu, and J.-L. Bocquet. Resistivity recovery simulations of electron-irradiated iron: Kinetic Monte Carlo versus cluster dynamics. *J Nucl Mater*, 352:42, 2006.
- [7] I. Martin-Bragado, A. Rivera, G. Valles, J. L. Gomez-Selles, and M. J. Caturla. MMonCa: An Object Kinetic Monte Carlo simulator for damage irradiation evolution and defect diffusion. *Comput. Phys. Commun.*, 184(12):2703, 2013.
- [8] E. Martinez, M. J. Caturla, and J. Marian. *DFT-Parameterized Object Kinetic Monte Carlo Simulations of Radiation Damage*, page 2457. Springer International Publishing, 2020.
- [9] N. M. Ghoniem, S. H. Tong, J. Huang, B. N. Singh, and M. Wen. Mechanisms of dislocation-defect interactions in irradiated metals investigated by computer simulations. *J. Nucl. Mater.*, 307-311:843, 2002.
- [10] A. B. Sivak, V. M. Chernov, V. A. Romanov, and P. A. Sivak. Kinetic Monte-Carlo simulation of self-point defect diffusion in dislocation elastic fields in bcc iron and vanadium. *J. Nucl. Mater.*, 417:1067, 2011.
- [11] G. Subramanian, D. Perez, B. P. Uberuaga, C. N. Tomé, and A. F. Voter. Method to account for arbitrary strains in kinetic Monte Carlo simulations. *Phys. Rev. B*, 87:144107, 2013.
- [12] A. Vattré, T. Jourdan, H. Ding, M.-C. Marinica, and M. J. Demkowicz. Non-random walk diffusion enhances the sink strength of semicoherent interfaces. *Nat. Commun.*, 7:10424, 2016.
- [13] D. Carpentier, T. Jourdan, Y. Le Bouar, and M.-C. Marinica. Effect of saddle point anisotropy of point defects on their absorption by dislocations and cavities. *Acta Mater.*, 136:323, 2017.
- [14] T. Jourdan and A. Vattré. A continuous model including elastodiffusion for sink strength calculation of interfaces. *Comput. Mater. Sci.*, 153:473, 2018.
- [15] D. R. Mason, X. Yi, M. A. Kirk, and S. L. Dudarev. Elastic trapping of dislocation loops in cascades in ion-irradiated tungsten foils. *J. Phys.: Condens. Matter*, 26:375701, 2014.
- [16] D. Carpentier, T. Jourdan, P. Terrier, M. Athènes, and Y. Le Bouar. Effect of sink strength dispersion on cluster size distributions simulated by cluster dynamics. *J. Nucl. Mater.*, 533:152068, 2020.
- [17] A. A. Kohnert and L. Capolungo. Sink strength and dislocation bias of three-dimensional microstructures. *Phys. Rev. Mater.*, 3:053608, 2019.
- [18] H. Moulinec and P. Suquet. A fast numerical method for computing the linear and nonlinear mechanical properties of composites. *C. R. Acad. Sci. Paris, Ser. II*, 318:1417, 1994.
- [19] S. Y. Hu and L. Q. Chen. Solute segregation and coherent nucleation and growth near a dislocation – a phase-field model integrating defect and phase microstructures. *Acta Mater.*, 49:463, 2001.
- [20] D. Rodney, Y. Le Bouar, and A. Finel. Phase field methods and dislocations. *Acta Mater.*, 51:17, 2003.
- [21] N. Bertin, M. V. Upadhyay, C. Pradalier, and L. Capolungo. A FFT-based formulation for efficient mechanical fields computation in isotropic and anisotropic periodic discrete dislocation dynamics. *Modell. Simul. Mater. Sci. Eng.*, 23:065009, 2015.

- 744 [22] J. T. Graham, A. D. Rollett, and R. LeSar. Fast Fourier transform discrete dislocation dynamics.
745 *Modell. Simul. Mater. Sci. Eng.*, 24:085005, 2016.
- 746 [23] R. LeSar and L. Capolungo. *Advances in Discrete Dislocation Dynamics Simulations*, page 1079.
747 Springer International Publishing, 2020.
- 748 [24] L. Greengard and V. Rokhlin. Rapid evaluation of potential fields in three dimensions. In
749 C. Anderson and C. Greengard, editors, *Vortex Methods*, volume 1360 of *Lectures Notes in*
750 *Mathematics*, page 121. Springer-Verlag, Berlin, 1988.
- 751 [25] H. Cheng, L. Greengard, and V. Rokhlin. A fast adaptive multipole algorithm in three dimensions.
752 *J. Comput. Phys.*, 155:468, 1999.
- 753 [26] A. Arsenlis, W. Cai, M. Tang, M. Rhee, T. Opplestrup, G. Hommes, T. G. Pierce, and V. V.
754 Bulatov. Enabling strain hardening simulations with dislocation dynamics. *Modelling Simul.*
755 *Mater. Sci. Eng.*, 15:553, 2007.
- 756 [27] D. Zhao, J. Huang, and Y. Xiang. A new version fast multipole method for evaluating the stress
757 field of dislocation ensembles. *Modelling Simul. Mater. Sci. Eng.*, 18:045006, 2010.
- 758 [28] C. Chen, S. Aubry, T. Ooppelstrup, A. Arsenlis, and E. Darve. Fast algorithms for evaluating the
759 stress field of dislocation lines in anisotropic elastic media. *Modell. Simul. Mater. Sci. Eng.*,
760 26:045007, 2018.
- 761 [29] Daniel T. Gillespie. A general method for numerically simulating the stochastic time evolution of
762 coupled chemical reactions. *J. Comput. Phys.*, 22:403, 1976.
- 763 [30] A. B. Bortz, M. H. Kalos, and J. L. Lebowitz. A New Algorithm for Monte-Carlo Simulation of
764 Ising Spin Systems. *J. Comput. Phys.*, 17:10, 1975.
- 765 [31] T. Jourdan. Enforcing local equilibrium of point defects near sinks in object kinetic monte carlo
766 simulations. *Modell. Simul. Mater. Sci. Eng.*, 29:035007, 2021.
- 767 [32] R. Siems. Mechanical interactions of point defects. *Phys. Stat. Sol.*, 30:645, 1968.
- 768 [33] E. Clouet, C. Varvenne, and T. Jourdan. Elastic modeling of point-defects and their interactions.
769 *Comp. Mater. Sci.*, 147:49, 2018.
- 770 [34] N. M. Ghoniem and L. Z. Sun. Fast-sum method for the elastic field of three-dimensional
771 dislocation ensembles. *Phys. Rev. B*, 60:128, 1999.
- 772 [35] J. P. Hirth and J. Lothe. *Theory of dislocations*. McGraw-Hill, 1968.
- 773 [36] T. Mura. *Micromechanics of defects in solids*. Martinus Nijhoff, 1987.
- 774 [37] W. G. Wolfer and M. Ashkin. Stress-induced diffusion of point defects to spherical sinks. *J. Appl.*
775 *Phys.*, 46:547, 1975.
- 776 [38] V. A. Borodin, A. I. Ryazanov, and C. Abromeit. Void bias factors due to the anisotropy of the
777 point defect diffusion. *J. Nucl. Mater.*, 207:242, 1993.
- 778 [39] N. A. Gumerov and R. Duraiswami. Fast multipole method for the biharmonic equation in three
779 dimensions. *J. Comput. Phys.*, 215:363, 2006.
- 780 [40] H. Y. Wang and R. LeSar. An efficient fast-multipole algorithm based on an expansion in the
781 solid harmonics. *J. Chem. Phys.*, 104:4173, 1996.
- 782 [41] C. H. Choi, J. Ivanic, M. S. Gordon, and K. Ruedenberg. Rapid and stable determination of
783 rotation matrices between spherical harmonics by direct recursion. *J. Chem. Phys.*, 111:8825,
784 1999.
- 785 [42] G. B. Arfken and H. J. Weber. *Mathematical Methods for Physicists*. Elsevier, 2005.
- 786 [43] Y. Fu, K. J. Klimkowski, G. J. Rodin, E. Berger, J. C. Browne, J. K. Singer, R. A. van de Geijn,
787 and K. S. Vemaganti. A fast solution method for three-dimensional many-particle problems of
788 linear elasticity. *Int. J. Numer. Meth. Eng.*, 42:1215, 1998.
- 789 [44] Y. Fu and G. J. Rodin. Fast solution method for three-dimensional Stokes many-particle problems.
790 *Commun. Numer. Meth. Eng.*, 16:145, 2000.
- 791 [45] T. Jourdan, F. Lançon, and A. Marty. Pinning of magnetic domain walls to structural defects in
792 thin layers within a Heisenberg-type model. *Phys. Rev. B*, 75:094422, 2007.
- 793 [46] C. G. Lambert, T. A. Darden, and J. A. Board Jr. A multipole-based algorithm for efficient
794 calculation of forces and potentials in macroscopic periodic assemblies of particles. *J. Comput.*

795 *Phys.*, 126:274, 1996.

- 796 [47] W. Cai, V. V. Bulatov, J. Chang, J. Li, and S. Yip. Periodic image effects in dislocation modelling.
797 *Philos. Mag.*, 83(5):539, 2003.
- 798 [48] T. Jourdan. Simulation of macroscopic systems with non-vanishing elastic dipole components. *J.*
799 *Mech. Phys. Solids*, 125:762, 2019.
- 800 [49] G. Leibfried and N. Breuer. Point Defects in Metals I. In *Springer Tracts in Modern Physics*.
801 Springer-Verlag, Berlin, 1978.
- 802 [50] E. van der Giessen and A. Needleman. Discrete dislocation plasticity: a simple planar model.
803 *Modelling Simul. Mater. Sci. Eng.*, 3:689, 1995.
- 804 [51] D. Braess. *Finite elements : Theory, fast solvers, and applications in solid mechanics*. Cambridge
805 University Press, 1997.
- 806 [52] F. Baraglia and P.-W. Ma. Dynamic model for an ensemble of interacting irradiation-induced
807 defects in a macroscopic sample. *Modell. Simul. Mater. Sci. Eng.*, 29:025004, 2021.
- 808 [53] M. Kuchta, K.-A. Mardal, and M. Mortensen. On the singular Neumann problem in linear
809 elasticity. *Numer. Linear Algebra Appl.*, 26(1):e2212, 2019.
- 810 [54] M. S. Alnæs, J. Blechta, J. Hake, A. Johansson, B. Kehlet, A. Logg, C. Richardson, J. Ring, M. E.
811 Rognes, and G. N. Wells. The FEniCS Project Version 1.5. *Archive of Numerical Software*,
812 3(100):9, 2015.
- 813 [55] C. Geuzaine and J.-F. Remacle. Gmsh: a three-dimensional finite element mesh generator with
814 built-in pre- and post-processing facilities. *Int. J. Numer. Methods Eng.*, 79(11):1309, 2009.
- 815 [56] H. L. Heinisch, B. N. Singh, and S. I. Golubov. The effects of one-dimensional glide on the reaction
816 kinetics of interstitial clusters. *J. Nucl. Mater.*, 283–287:737, 2000.
- 817 [57] A. Seeger and U. Gösele. Steady-state diffusion of point defects to dislocation loops. *Phys. Lett.*
818 *A*, 61:423, 1977.
- 819 [58] B. Vigholm and M. J. Makin. The effect of solute concentration on the formation of loops in
820 aluminium-magnesium alloys during fission fragment irradiation. *Phys. Stat. Sol.*, 12:877, 1965.
- 821 [59] D. I. R. Norris. The use of the high voltage electron microscope to simulate fast neutron-induced
822 void swelling in metals. *J. Nucl. Mater.*, 40:66, 1971.
- 823 [60] K. Ma, B. Décamps, A. Fraczkiewicz, T. Jourdan, F. Prima, and M. Loyer-Prost. Free surface
824 impact on radiation damage in pure nickel by in-situ self-irradiation: can it be avoided? *Acta*
825 *Mater.*, 212:116874, 2021.
- 826 [61] A. Barbu, C. S. Becquart, J.-L. Bocquet, J. Dalla Torre, and C. Domain. Comparison between
827 three complementary approaches to simulate ‘large’ fluence irradiation: application to electron
828 irradiation of thin foils. *Philos. Mag.*, 85:541, 2005.
- 829 [62] K. Urban. Growth of defect clusters in thin nickel foils during electron irradiation. *Phys. Stat.*
830 *Sol. (a)*, 4:761, 1971.
- 831 [63] M. Kiritani, N. Yoshida, H. Takata, and Y. Maehara. Growth of interstitial type dislocation loops
832 and vacancy mobility in electron irradiated materials. *J. Phys. Soc. Jpn*, 38(6):1677, 1975.
- 833 [64] S. Jitsukawa and K. Hojou. Effect of temperature and flux change on the behavior of radiation
834 induced dislocation loops in pure aluminum. *J. Nucl. Mater.*, 212-215:221–225, 1994.
- 835 [65] R. Bullough, D. W. Wells, J. R. Willis, and M. H. Wood. The interaction energy between
836 interstitial atoms and dislocations and its relevance to irradiation damage processes. In M. F.
837 Ashby, R. Bullough, C. S. Hartley, and J. P. Hirth, editors, *Dislocation Modelling of Physical*
838 *Systems*, page 116. Pergamon, 1981.
- 839 [66] H. Rouchette, L. Thuinet, A. Legris, A. Ambard, and C. Domain. Numerical evaluation of
840 dislocation loop sink strengths: A phase-field approach. *Nucl. Instr. Meth. B*, 352:31, 2015.
- 841 [67] D. Carpentier. *Simulation of the absorption kinetics of point defects by dislocations and defect*
842 *clusters*. PhD thesis, Université Paris-Saclay, 2018.
- 843 [68] R. J. A. Tough and A. J. Stone. Properties of the regular and irregular solid harmonics. *J. Phys.*
844 *A: Math. Gen.*, 10:1261, 1977.